Advanced Functional Materials

ADVANCED FUNCTIONAL MATERIALS
www.afm-journal.de

RESEARCH ARTICLE

Carbon Confinement as a Design Principle for Multiphase Magnetic Nanocomposites With Broadband Functionality

Shah Qasim Jan[1] | Rajeswari Roy Chowdhury[1] | Noah Schulz[2] | Ayomipo Israel Ojo[1] | María González de la Vega[3] | Jesús A. Blanco[3] | Pedro Gorria[3,4] | Darío A. Arena[1] | Hariharan Srikanth[1]

[1]Department of Physics, University of South Florida, Tampa, Florida, USA | [2]Naval Surface Warfare Center, Panama City, USA | [3]Departamento De Física, Universidad De Oviedo, Oviedo, Spain | [4]IUTA, Universidad De Oviedo, Gijón, Spain

Correspondence: Pedro Gorria (pgorria@uniovi.es) | Darío A. Arena (darena@usf.edu) | Hariharan Srikanth (sharihar@usf.edu)

Received: 19 November 2025 | **Revised:** 8 January 2026 | **Accepted:** 27 January 2026

Keywords: ferromagnetic resonance | magnetic anisotropy | magnetic hyperthermia | magnetic nanocomposites | specific absorption rate | transverse susceptibility | wasp-waisted hysteresis loop

ABSTRACT

While broadband electromagnetic (EM) loss mechanisms have critical implications for both electromagnetic absorbers and magnetic hyperthermia, integrating diverse loss channels into single material architecture remains a key challenge for next-generation multifunctional composites. Herein, we introduce carbon confinement of Cobalt Ferrite nanoparticles (CFO@C) as a design principle to simultaneously address the performance-processability trade-off for broadband functionality. Mesoporous activated carbon acts as a reactive template that constrains CFO nanoparticle growth ($\sim$ 8 nm), mitigates agglomeration, and provides conductive pathways for complementary dielectric response (ε). Static magnetometry reveals complex magnetic behavior driven by coexisting hard and soft phases, which is quantitatively resolved using Voigt-profile deconvolution of the wasp-waisted hysteresis loops, enabling phase-resolved analysis of reversal processes. Ferromagnetic Resonance (18–30 GHz) reveals a stable g-factor and large damping ($\alpha = 0.14$) indicative of efficient GHz-frequency energy dissipation governed by spin–lattice relaxation. Low-frequency magnetic hyperthermia validates linear-response relaxation as the dominant loss channel under physiological field conditions (310 kHz, 400–800 Oe). These results establish CFO@C as a multifunctional nanocomposite that unifies broadband EM dissipation with efficient low-frequency heating, establishing the pathway for $\mu - \varepsilon$ co-design in frequency-adaptive materials relevant to printed electronics, EMI mitigation, and magnetically driven functional devices.

1 | Introduction

The development of functional materials increasingly demands precise control over physical properties across diverse length scales and operating frequencies. Magnetic nanocomposites offer unique advantages in this regard, enabling tailored responses suitable for applications ranging from biomedicine to advanced electronics [1, 2]. Among these materials, spinel ferrites such as cobalt ferrite (CFO) have emerged as promising candidates owing to their high chemical stability, moderate saturation magnetization, and tunable magnetic anisotropy [3]. However, the practical implementation of these nanoparticles often faces challenges related to agglomeration, mixed oxidation, and limited dispersion in functional matrices [4, 5]. To address these limitations, embedding magnetic nanoparticles (MNPs) within a carbon-based matrix, especially one offering structural confinement and chemical protection, has proven to be a highly effective strategy [6–8]. From an applications standpoint, many industrial electromagnetic (EM) absorbers draw on two of the complementary material classes, carbonaceous media that dissipate via dielectric/conductive loss and ferrites that dissipate via magnetic loss, forming the backbone of commercial EMI shielding and

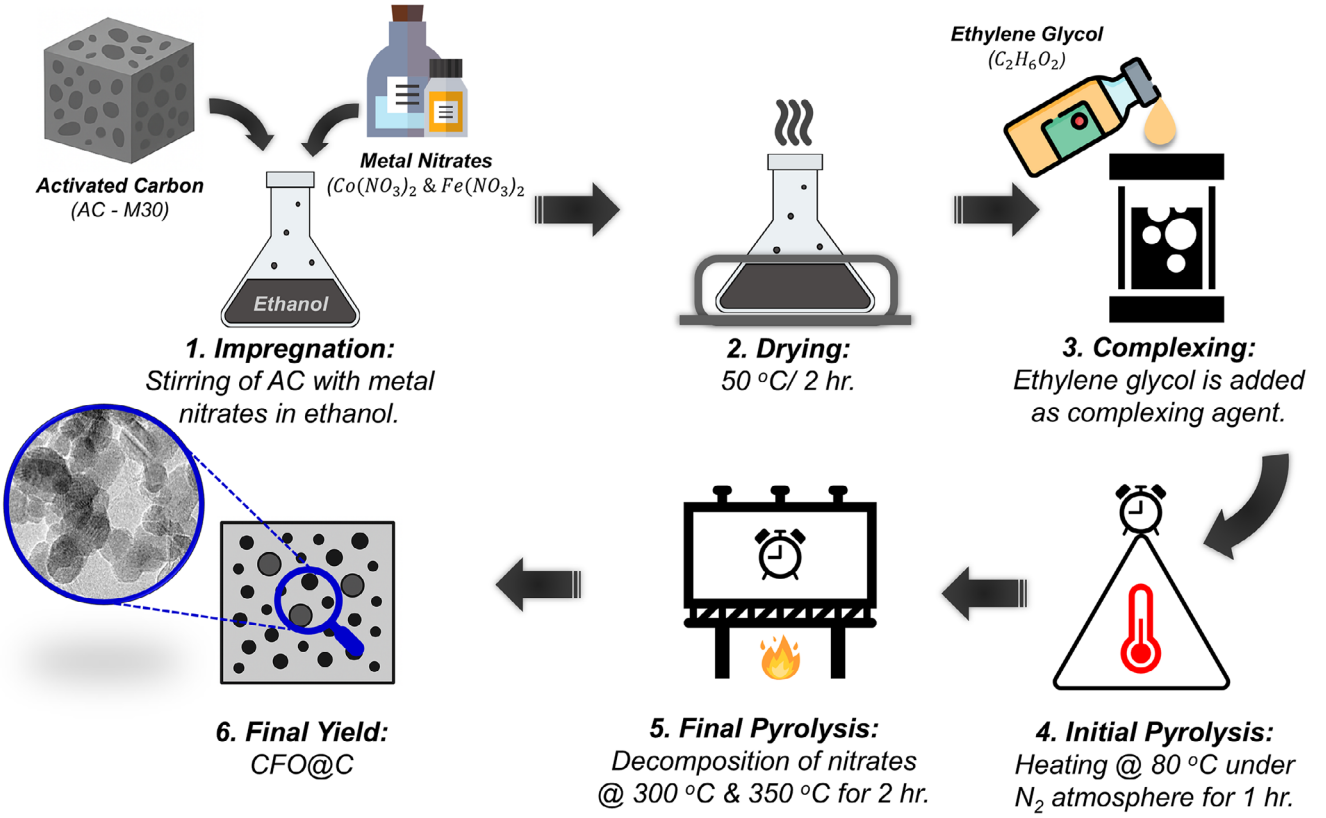

FIGURE 1 | Schematic illustration of the synthesis protocol for cobalt ferrite nanoparticles embedded within an activated carbon matrix (CFO@C).

radar-absorbent technologies [9, 10]. Integrating both channels into a single, co-engineered composite is therefore attractive for attaining stronger, broader-band attenuation with thinner layers [11].

Carbon-based matrices, including graphene, carbon nanotubes, and activated carbon, are attractive platforms for electromagnetic absorber design due to their low density, chemical stability, and ability to host magnetic nanoparticles in a controlled and spatially confined manner [12–16]. Among these, activated carbon offers a porous framework that suppresses nanoparticle aggregation during thermal processing while enabling precise control over particle size and phase evolution, both of which are critical for tuning magnetic responses across different frequency regimes [17–20]. In composite absorbers, porous carbons primarily regulate the complex permittivity (ε', ε'') through conductive pathways and interfacial polarization, whereas nanoscale ferrites govern the complex permeability (μ', μ'') via resonance and domain-related loss processes [21–23]. Co-design of both the dielectric and magnetic contributions allows impedance matching to be achieved while maintaining strong intrinsic loss. Recent studies have further shown that the carbon environment plays an active role in shaping magnetic behavior by modulating interfacial coupling, surface anisotropy, and phase stability in carbon embedded nanoparticles, providing an additional degree of freedom for engineering broadband electromagnetic functionality [24, 25].

Herein, we report the synthesis of CFO nanoparticles within a porous activated carbon matrix (Figure 1), a composite architecture designed to exploit the advantages of both the multiphase magnetic part and the structural benefits of the carbon host for broadband electromagnetic functionality with relevance to EMI shielding, microwave absorption and additive manufacturing for frequency selective devices. Such multiphase systems, particularly those incorporating both hard and soft magnetic components, are known to exhibit unique magnetization dynamics and enhanced broadband magnetic loss mechanisms due to exchange coupling phenomena, critical for high-frequency applications [26]. Through comprehensive magnetic characterizations spanning distinct frequency regimes of radio spectrum, including static magnetization measurements, Medium Frequency (MF) calorimetric hyperthermia (kHz), High Frequency (HF) transverse susceptibility (MHz), and Super High Frequency (SHF) ferromagnetic resonance (GHz), we demonstrate that the combination of distinct magnetic phases and the confining carbon matrix supports tunable magnetic responses across a wide frequency range (from kHz to tens of GHz).

Overall, in our composite CFO@C system, carbon confinement enables a unified materials strategy in which magnetic permeability is tuned through controlled phase coexistence, while dielectric permittivity is independently regulated through the conductive and porous carbon scaffold. This decoupled yet cooperative control of μ and ε provides a direct design strategy toward impedance-matched, broadband electromagnetic dissipation across multiple frequency regimes. Beyond absorption, the same structural features, namely nanoscale confinement, multiphase magnetic response, and processable carbon frameworks, also position such composites for integration into frequency-adaptive shielding architectures and magnetically driven heating platforms, where tunable loss mechanisms are essential [27–29].

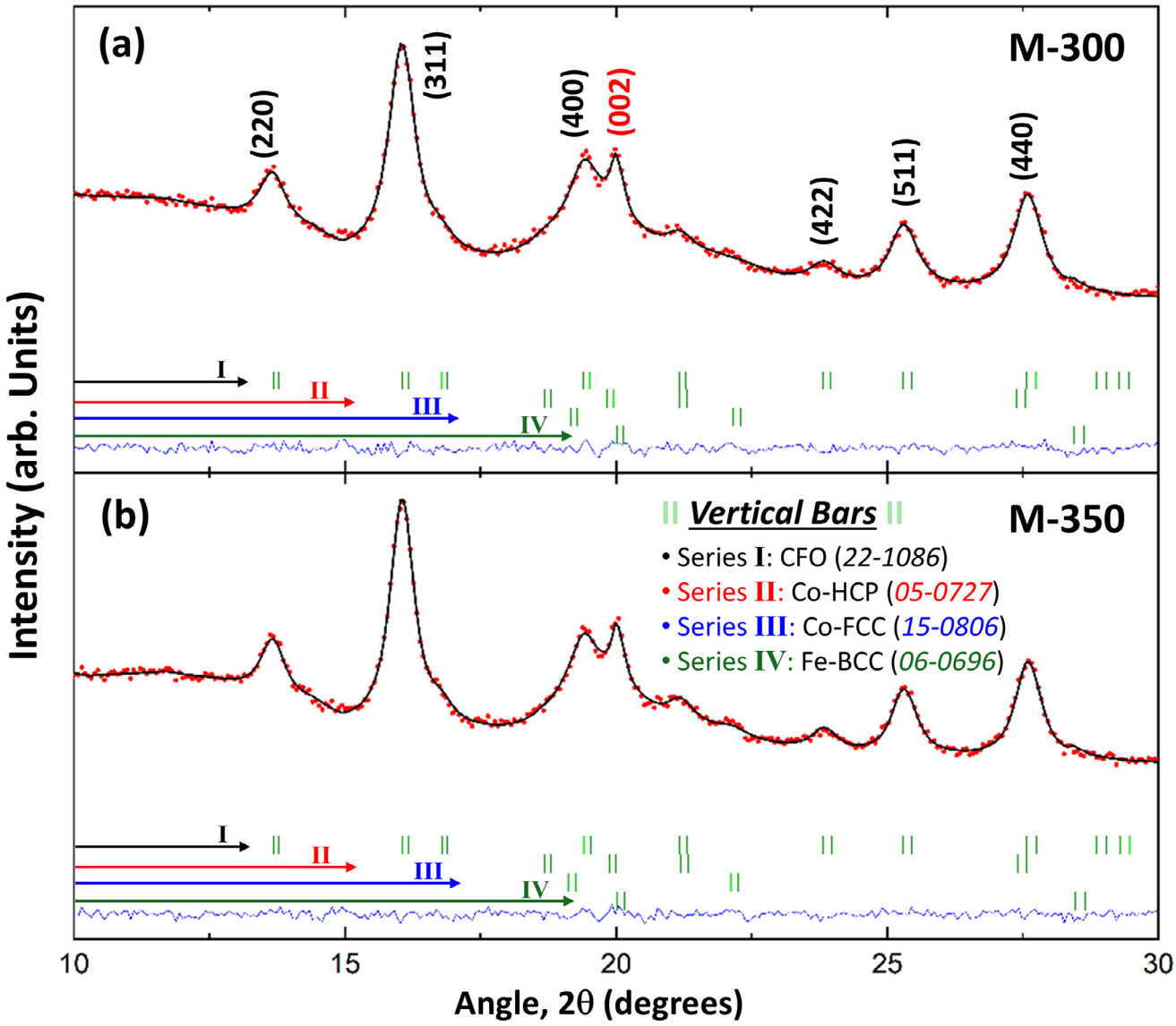

FIGURE 2 | Room temperature XRD patterns of samples (a) M-300 and (b) M-350, collected at room temperature in a Seifert XRD 3000 T/T diffractometer with Mo K_{α_1} (0.709 Å) and K_{α_2} (0.713 Å) radiations, in an angular range (2θ) of $10 - 30^{o}$ in steps of 0.03^{o}. Red dots represent experimental data, black lines show Rietveld fits, vertical green markers indicate the position of Bragg reflections and blue lines correspond to the difference between experimental and calculated patterns. The first series of vertical bars correspond to the position of the Bragg reflections associated with the crystal structure of CFO (JCPDS No. 22–1086), the second ones to the Co-HCP (JCPDS No. 05–0727), the third ones to the Co-FCC (JCPDS No. (15-0806) and the fourth ones to the Fe-BCC (< 2–3%) (JCPDS No. 06–0696) [32–35].

2 | Results and Discussion

2.1 | Structural and Microstructural Studies

Figure 2 shows the room temperature XRD patterns of the two samples along with the corresponding fits. The main Bragg reflections: (220), (311), (400), (422), (511) and (440) can be indexed according to the spinel-type crystal structure of CFO (standard JCPDS Card No. 22–1086), described in terms of a face centered (FCC) unit cell with space group $Fd\bar{3}m$ (No. 227) [32]. The value of the refined lattice parameters was found to be a = 8.420(2) for M-300 and a = 8.418(1) Å for M-350, values consistent with those reported for bulk $CoFe_2O_4$ [26]. Besides the reflections of the CFO crystal structure, a small amount of metallic Co (≈ 20%) is needed to properly fit the patterns, particularly near the (400) Bragg reflection at around 20° in 2θ. The observed background signal that decreases with the 2θ angle comes from the amorphous carbon matrix. From the analysis of the broadening of the diffraction peaks, the average crystallite sizes were estimated to be ∼ 6.5 nm for M-300 and ∼ 7.5 nm for M-350.

Representative TEM and HRTEM images of the M-300 sample together with the size histogram can be shown in Figure 3, where quasi-spherical NPs are clearly identified. From the NP size histogram and the fit to a lognormal distribution [see Figure 3b], we have also estimated the average value of the NP diameter (D_{TEM} = 8 nm) and the standard deviation (σ = 2 nm). These values coincide, within the experimental error, with those

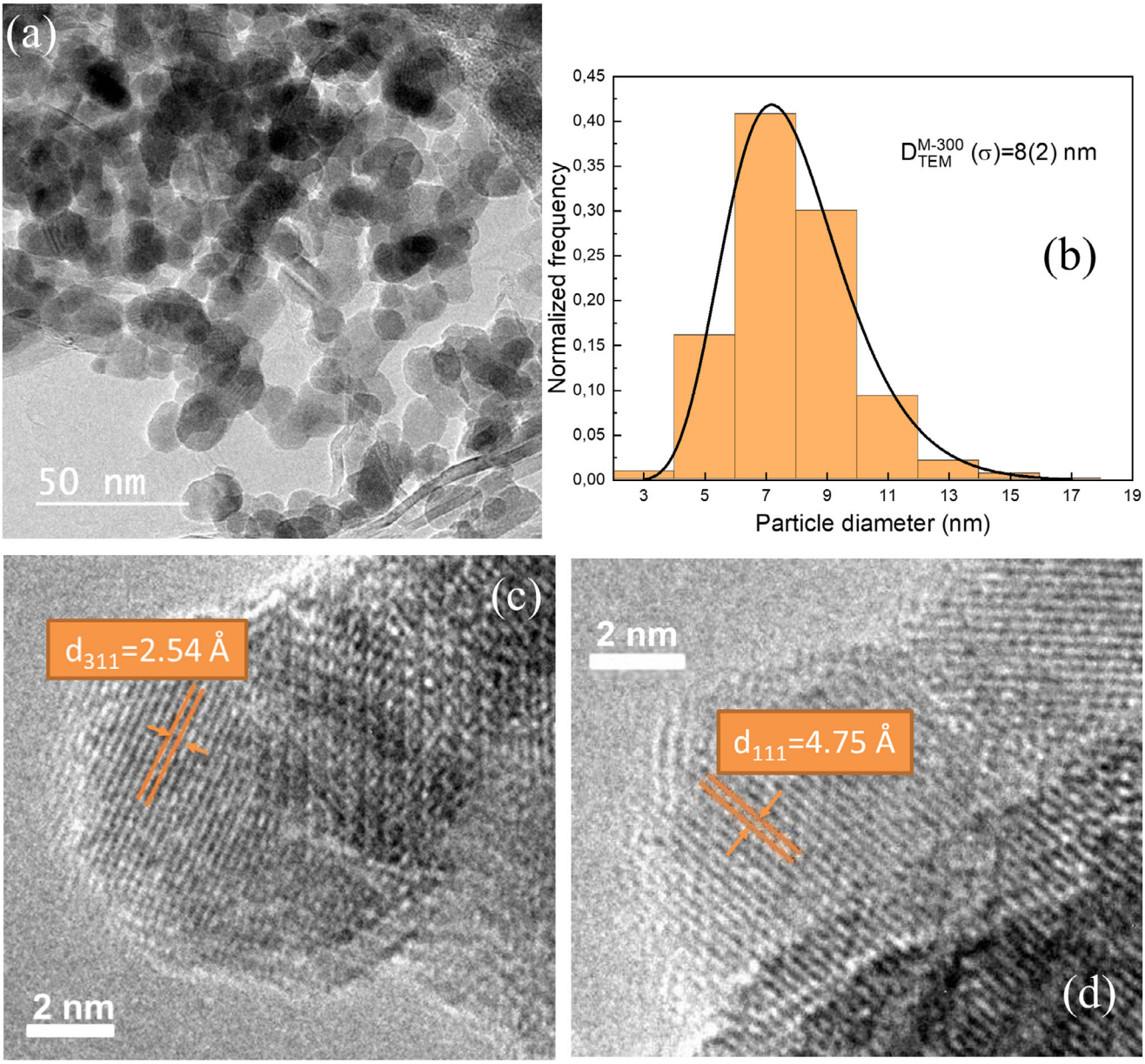

FIGURE 3 | (a) TEM image of the NPs revealing their almost-spherical morphology. (b) Histogram of the NP diameter together with the best-fit log-normal distribution (black solid line), characterized by the mean diameter (D_{TEM}) and standard deviation (σ) parameters. (c,d) HRTEM images for individual NPs evidencing the (111) and (311) interplanar distances of the $CoFe_2O_4$ crystalline structure.

obtained for the sample M-350 and are also consistent with the crystallite sizes estimated from the XRD analysis. By examining the HRTEM images [Figure 3c,d], there is clear evidence of the NP crystallinity. Measured interplanar spacings of 2.54 and 4.75 Å correspond to the (311) and (111) reflections, respectively. Taken together, the TEM/HRTEM and XRD results indicate that both samples exhibit similar structural and morphological characteristics.

2.2 | Static Magnetic Studies

To investigate the intrinsic magnetic properties and the temperature evolution of magnetization in the CFO@C nanocomposites, static magnetization measurements were performed on the two samples, M-300 and M-350. The temperature dependence of magnetization, M(T) curves, was investigated using ZFC, FC, and FCW protocols for the representative samples under an applied field of 100 Oe. M(T) curves for the sample M-350 are presented in Figure 4a and Figure S2a. As can be seen in the figure that the ZFC-FC curves exhibit a well-defined bifurcation. For both M-300 and M-350, the magnetization in the ZFC curves increases with temperature, forming a broad, diffused hump that extends approximately from 250 K up to 350 K. This broad peak suggests a wide distribution of blocking temperatures, T_B, within the nanoparticle ensemble, This distribution arises from two primary factors: (1) the polydispersity in particle size observed from TEM analysis (see Figure 2), and (2) the presence of distinct magnetic phases, likely stemming from variations in composition and crystallinity as evidenced from the XRD analysis. Each of these

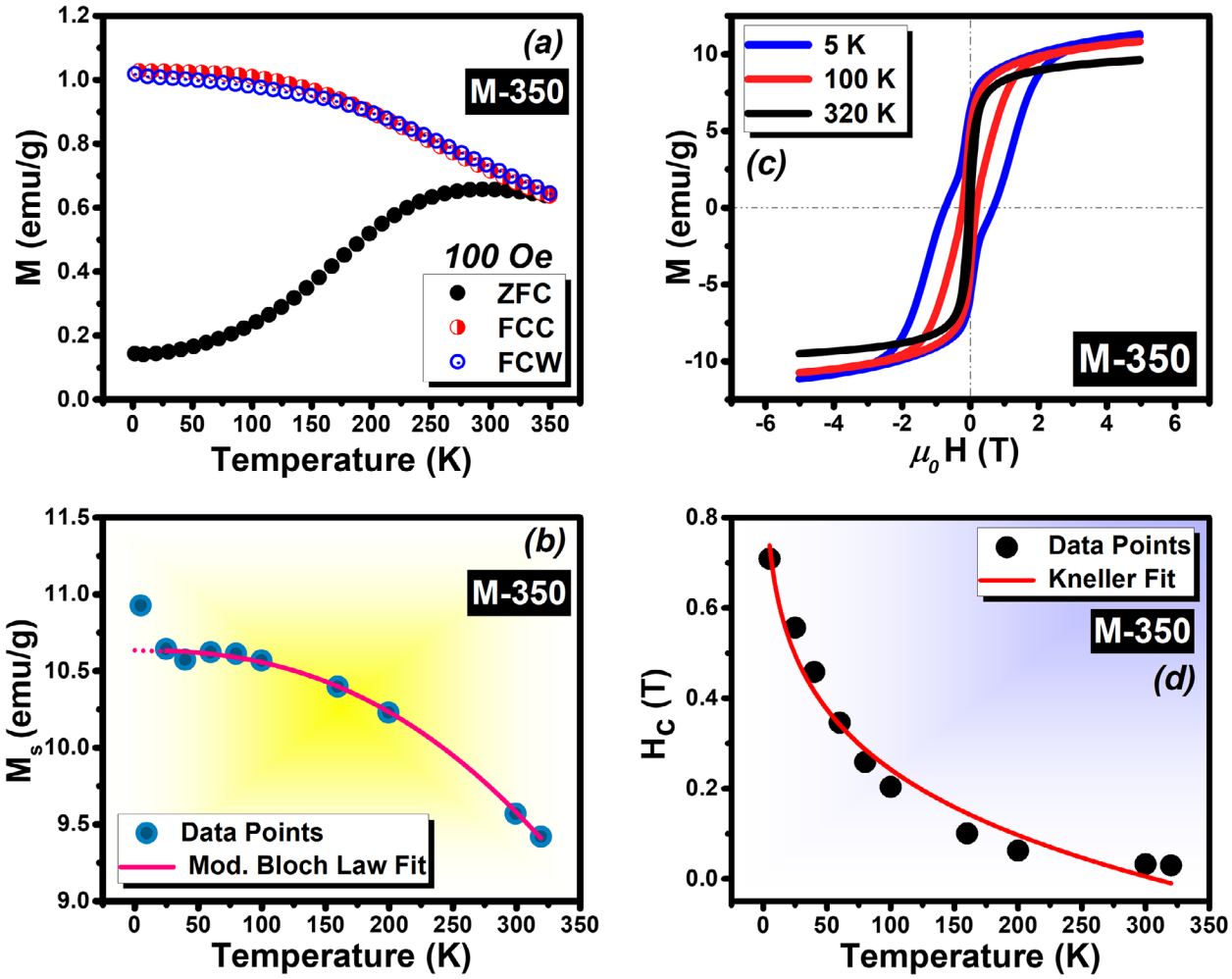

FIGURE 4 | (a) Magnetization vs. temperature curves, (b) Bloch fitting of saturation magnetization (M_s) vs. temperature, and (c) M(H) curves at different selected temperatures, (d) Modified Kneller law fitting of the coercivity (H_c) vs. temperature data of M-350.

phases would possess different magnetic anisotropy constants and intrinsic Curie temperatures, leading to a broad, composite distribution of blocking temperatures. In this temperature range, as thermal energy increases, nanoparticles transition from a blocked, anisotropic state to a superparamagnetic state, where their moments rapidly fluctuate and align with the external field [36]. The diffused nature of the hump, rather than a sharp peak, further supports a broad distribution of magnetic anisotropy energies across the varied particle sizes and potentially different magnetic phases present.

At low temperatures, specifically below ~ 25 K, the ZFC curve exhibits an upward trend, forming a subtle feature, rather than a sharp peak or plateau commonly associated with uniform blocking. This low-temperature behavior, although less pronounced, suggests the emergence of additional magnetic complexities. This upward turn in ZFC at cryogenic temperatures, coupled with the continued divergence from the FC curve, is often associated with the onset of spin-glass-like behavior or a cluster-glass transition [37]. Such phenomena in nanoparticle systems typically arise from either highly disordered spins at the nanoparticle surfaces (surface spin canting/disorder) or weak, frustrated interparticle interactions among the randomly dispersed nanoparticles within the carbon matrix [38]. Given the ~ 20 wt.% CFO loading, interparticle interactions, even if subtle, are plausible. Furthermore, the multiphases (CFO, Co-FCC, Co-HCP) could introduce complex interfacial exchange interactions contributing to this low-temperature freezing.

To further investigate the intrinsic magnetic properties, the temperature dependence of the saturation magnetization, extracted from M(H) data (as shown in Figure 3c and Figure S2b,c), was analyzed. The M_s vs. T data was fitted using the Bloch law as follows [39].

$$M_s\ (T) = M_{s_0}\left[1 - \beta T^{\alpha}\right] \quad (1)$$

where $M_s(T)$ is the saturation magnetization at temperature T, M_{s_0} is the saturation magnetization at temperature $T = 0$ K, β is the Bloch constant and α is Bloch exponent (typically 3/2 for bulk materials and greater than 3/2 for nanoparticles system. For our case, the value of α acquired from the fit is 2.38 $\pm$ 0.12, which agrees with the already reported results: 0.83 − 2.87 [40, 41]. As shown in Figure 4b and Figure S2e, a good fit to the Bloch law was obtained in the temperature range of 20 to 320 K for both the samples. However, the fit deviates in the sub 10 K regime, failing to account for the magnetic behavior in this region. This deviation relates to the low-temperature observations in the ZFC

curve, indicating that the magnetic ordering is dominated by contributions from disordered surface spins or collective freezing into a glassy state, where the fundamental assumptions of the Bloch law no longer hold [42, 43].

To gain further insights into magnetic anisotropy and its temperature dependence of the CFO@C nanocomposites, we employed Kneller law, which describes the temperature dependence of coercivity for systems approaching superparamagnetic relaxation. The experimental data for coercivity $H_C(T)$ as a function of temperature was fitted using the modified Kneller equation as:

$$H_C(T) = H_{C_0}\left[1 - \left[\frac{T}{T_B}\right]^{\delta}\right] \quad (2)$$

where H_{C_0} is the coercivity extrapolated to 0 K, T_B is the average blocking temperature, and δ is a dimensionless exponent that characterizes the type of magnetic interactions and domain structure. For ideal, non-interacting single-domain ferromagnetic particles, $\delta = 0.5$ is typically expected [41].

In our case, the Kneller fitting to the experimental $H_C(T)$ data over the range of 5–320 K (Figure 4d and Figure S2d) yielded average blocking temperature of $T_B = 307.7 \pm 35.3$ K and 306. 9 ± 36.2 K, with $\delta = 0.14 \pm 0.09$ and 0.13 ± 0.09, for the respective samples. The reduced value of δ suggests a deviation from ideal single-domain behavior, likely due to the fact that the magnetic reversal mechanism in our CFO@C nanocomposite system is more complex than a simple single-domain model. The lower δ value typically indicates the presence of interparticle interactions and/or non-uniform magnetic anisotropy [44, 45]. Given the multiphase nature of our system (CFO, Co-FCC, and Co-HCP), a distribution of particle sizes and magnetic anisotropies, as well as exchange or dipolar interactions between the constituent phases embedded within the carbon matrix, could lead to this reduced δ value [46, 47]. This finding further complements the insights gained from the Bloch law analysis, where deviations at low temperatures suggested collective or disordered spin states not accounted for by ideal ferromagnetic models.

Further insights into the complex magnetic interactions and the contributions of individual magnetic phases to the overall magnetic behavior were obtained through the deconvolution of the M(H) loops. For both M-300 and M-350 samples, the as-acquired M(H) loops exhibited a pronounced wasp-waisted shape (Figure 5b and Figure S2b,c,f), which is characteristic of systems comprising multiple magnetic phases with distinct coercivities or exchange interactions [48]. Such wasp-waisted features were analyzed using a peak-resolved approach applied to the differential susceptibility curves (dM/dH vs H).

The deconvolution was carried out by fitting the dM/dH data with a sum of two Voigt profiles, representing the respective hard and soft magnetic phases. The Voigt function is a convolution of a Gaussian and a Lorentzian profile and is expressed as:

$$V(x;\sigma,\gamma) = \int_{-\infty}^{\infty} G(x';\sigma)\, L(x-x';\gamma)\, dx' \quad (3)$$

where $G(x;\sigma) \equiv \frac{e^{-x^2/2\sigma^2}}{\sigma\sqrt{2\pi}}$ and $L(x;\gamma) \equiv \frac{\gamma}{\pi(x^2+\gamma^2)}$ denote the Gaussian and Lorentzian components, respectively, and σ and γ are the respective broadening parameters [49]. In our analysis, the soft phase corresponds to a narrow, tall peak in the dM/dH curve (indicating low coercivity), while the hard phase appears as a broad, shallow peak (higher coercivity), as shown in Figure 4a. The cumulative fit from both Voigt components accurately reconstructs the full dM/dH profile, validating the presence of two magnetically distinct contributions. By numerically integrating the individual Voigt-fitted components and reconstructing the respective magnetization curves, we successfully extracted the full M(H) response for the hard and soft phases, along with the total cumulative magnetization. As illustrated in Figure 5b and Figure S2f, the cumulative M(H) curve aligns excellently with the experimentally acquired hysteresis data, reinforcing the fidelity of the deconvolution method.

Figure 5c presents the temperature dependence of the coercive fields for M-350, derived from the Voigt-profile deconvolution (closed symbols). For comparison, the figure also shows experimental values obtained directly from the hysteresis loops (opened symbols). As can be seen, the decomposition separates the contributions of the soft and hard magnetic phases, whose individual trends with respect to temperature are shown. The cumulative $H_C(T)$ extracted from the fits closely follows the trend of the measured data, confirming the reliability of the deconvolution procedure. Minor deviations between the two are expected, as the fitting model treats the hard and soft components as magnetically independent, whereas in practice, interparticle interactions can modulate the effective switching field distribution. This analysis not only supports the structural and phase evidence of CFO coexisting with minor elemental Co phases (FCC and/or HCP) but also provides a quantitative handle on their magnetic switching characteristics.

Overall, the hysteresis-loop deconvolution provides a powerful framework for quantifying the relative contributions of these phases, enabling the strategic co-design of both permeability and permittivity to achieve optimal impedance matching and high intrinsic loss, both of which are prerequisites for strong, broadband absorption. In electromagnetic absorption and EMI shielding applications, the attenuation of incident radiation is governed by the combined response of electrical conductivity, dielectric permittivity, and magnetic permeability. While carbon-based materials primarily contribute to tailoring dielectric loss and electrical conductivity, magnetic permeability plays a decisive role in enabling magnetic loss and impedance matching. In the present system, the Voigt-profile based deconvolution reveals that permeability is not a fixed material constant in a composite system like ours, but an emergent property arising from the relative contributions of magnetically soft and hard phases. The soft magnetic component, associated with minor elemental Co phases, exhibits low coercivity and high susceptibility, leading to an enhanced magnetic response under low applied fields and contributing strongly to μ' and μ''. From an electromagnetic engineering perspective, this high differential permeability (dM/dH) suggests a tunable skin depth (δ), allowing for field-modulated attenuation profiles in low-frequency regimes. Conversely, the harder CFO phase introduces a broader distribution of anisotropy fields, stabilizing the magnetic response over extended field and

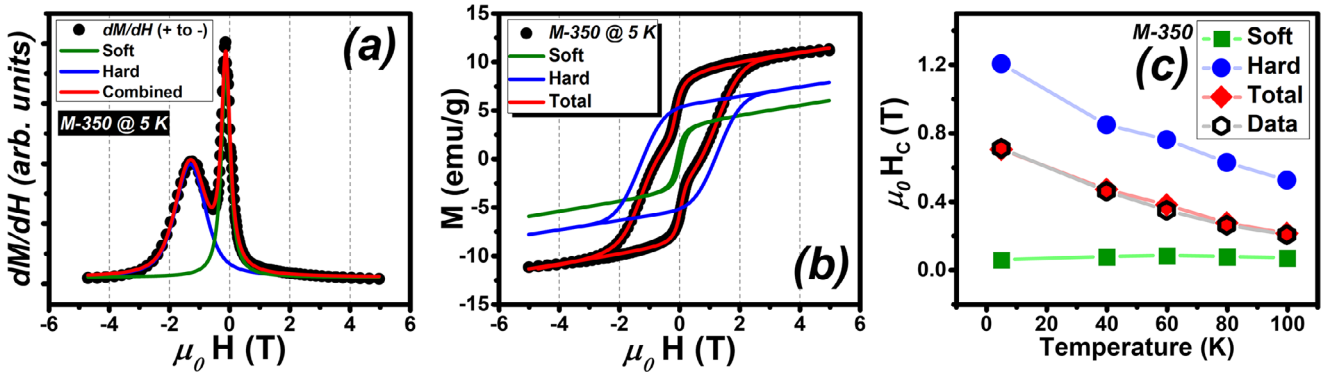

FIGURE 5 | Deconvolution of magnetic hysteresis (M(H)) loops data of M-350 taken at 5 K. (a) dM/dH curves with Voigt fits showing hard and soft magnetic phase contributions. (b) Reconstructed hard, soft, and cumulative M(H) loops overlaying the as-acquired experimental data. (c) Temperature dependence of the coercive field for M-350 extracted from Voigt-profile deconvolution of the hysteresis loops as well as those from the actual loops (experimental) data in the temperature range from 5 to 100 K.

frequency ranges. The ability to control this magnetic anisotropy opens pathways for designing angularly dependent absorbers, where electromagnetic response can be tailored based on the directional preference of the magnetization. Consequently, the coexistence of these phases therefore enables a permeability profile that is both responsive and spectrally distributed, a key requirement for broadband electromagnetic dissipation.

Additionally, the relative balance between these magnetic phases provides a direct materials-level handle to tune frequency-dependent loss mechanisms: increasing the fraction of the soft, metallic component enhances permeability and magnetic susceptibility, while higher oxidation states favor stability and broadened relaxation dynamics. This magnetic tunability is complemented by the activated carbon matrix, which operates at a different but equally critical level by governing dielectric permittivity and electrical conductivity. Rather than acting as a passive host, the porous carbon scaffold functions as an active template that not only constrains nanoparticle growth, suppresses aggregation, but also establishes conductive pathways that facilitate dielectric loss through interfacial polarization [12]. In addition, the mesoporous nature of the activated carbon matrix introduces effective air voids within the composite. Prior studies on hierarchical magnetic–dielectric systems with interfacial voids have shown that such structural features can act as impedance-matching mediators, improving input impedance and enabling deeper penetration of incident electromagnetic waves before dissipation within the magnetic core component [50]. Together, the combined control of μ through magnetic phase engineering and ε through carbon confinement enables impedance matching between free space and the composite, integrating magnetic and dielectric dissipation within a single, processable platform suitable for broadband electromagnetic attenuation.

2.3 | Dynamic Magnetic Properties and Frequency-Dependent Response

While static magnetic measurements provide essential insights into the fundamental magnetic state and phase contributions of the CFO@C nanocomposites, a comprehensive understanding of their suitability for advanced frequency-dependent applications, such as magnetic additive manufacturing and electromagnetic shielding, necessitates detailed characterization of their dynamic magnetic response across a broad range of frequencies. In this section, we present the results from transverse susceptibility, ferromagnetic resonance, and magnetic hyperthermia measurements, exploring the anisotropy, resonance, and energy dissipation mechanisms in the kHz to GHz range.

2.3.1 | Transverse Susceptibility

To probe the magnetic anisotropy and dynamic magnetic response of the CFO@C nanocomposites, TS measurements were performed on both the samples (M-300 and M-350) from 25 to 320 K. The advantage of this technique over conventional magnetometry approach lies in the fact that it detects the magnetic response of spins oriented perpendicular to an applied DC magnetic field. This selective sensitivity enables the identification of anisotropy fields as distinct features or singularities within the acquired TS curves [51]. The fundamental principles of TS for a single-domain uniaxial particle were initially formulated by Aharoni et al. in 1957, drawing upon the Stoner-Wohlfarth model. According to which, a theoretical TS curve, typically obtained during a unipolar field scan, is expected to exhibit three characteristic features/singularities. Two of these features correspond to the effective anisotropy field ($\mu_0 H_{K_{eff}}$), which is a summation of crystallographic and shape anisotropy contributions ($\mu_0 H_{K_{crystal}} + \mu_0 H_{K_{shape}}$) [52]. The third one is associated with the switching field. It is important to note that for systems comprising a collection of randomly oriented particles, the sharpness of these singular peaks may be diminished due to variations in H_K, yet they remain experimentally discernible. Importantly, TS can also be conceptualized as the zero-frequency limit of ferromagnetic resonance, thereby providing a complementary perspective on the system's dynamic magnetic behavior [51].

In our setup, a DC magnetic field was applied perpendicularly to the RF coil's axial field, ensuring transverse geometry. For measurement purposes, dried nanoparticles were placed in a gelatin capsule inside the coil (Schematics of the setup is shown in Figure 6a). The normalized transverse susceptibility, $\frac{\Delta\chi_T}{\chi_T}$, was

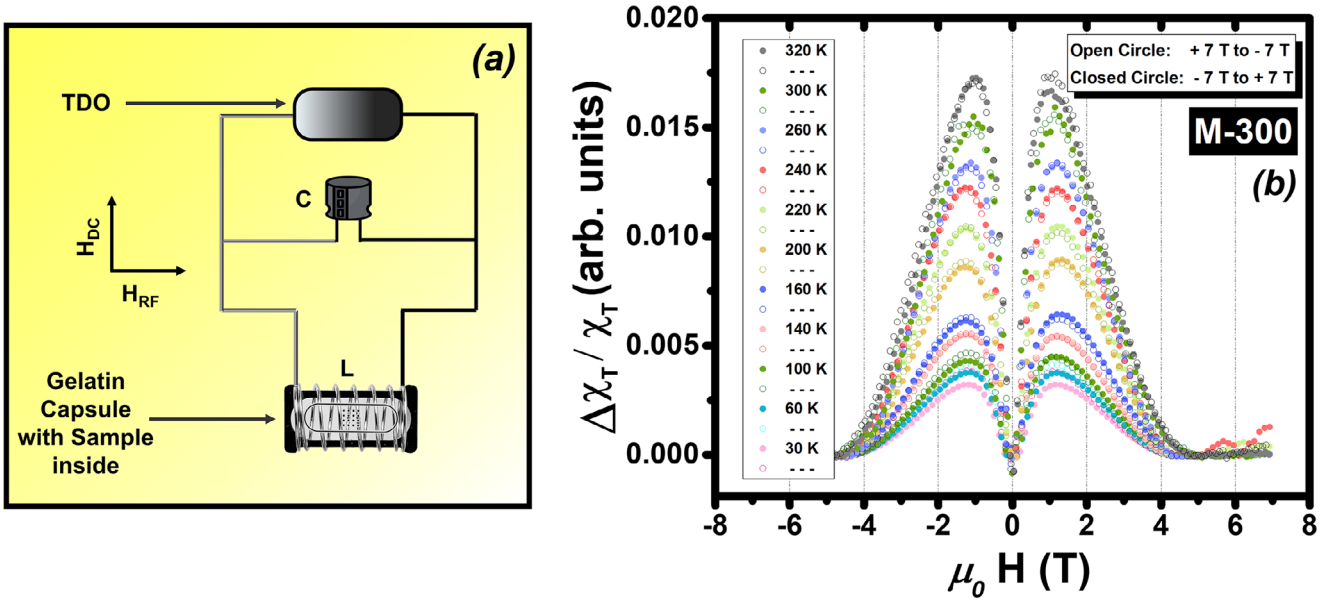

FIGURE 6 | (a) Schematics of the TS setup; (b) Temperature-dependent transverse susceptibility (TS) curves for CFO@C (M-300) nanocomposites.

obtained as a function of the applied DC field by measuring the resonant frequency shift of an LC tank circuit as the field was swept from positive to negative saturation, which is expressed as:

$$\frac{\Delta\chi_T}{\chi_T} = \frac{\left[\chi_T(H_{DC}) - \chi_{T_{DC}}^{SAT}\right]}{\chi_{T_{DC}}^{SAT}} \quad (4)$$

$\chi_T(H_{DC})$ in the above equation represents the transverse susceptibility, and $\chi_{T_{DC}}^{SAT}$ is the value of $\chi_T(H_{DC})$ at the saturation field.

Representative TS curves at various temperatures are shown in Figure 6b and Figure S3a. As can be seen, the TS curve for a single scan exhibit asymmetry in the anisotropy peaks. This asymmetry, previously observed in a 3D assembly of ferrite-based nanoparticle systems, demonstrated that the asymmetry in TS peak heights is highly sensitive to interparticle interactions [51]. They found that stronger dipolar interactions led to more symmetric peak heights, while weaker interactions resulted in greater asymmetry. In our CFO@C system, the observed asymmetry, particularly its temperature dependence, likely reflects the combined influence of some of the contributing factors, which may include multiphase interactions, where different magnetic phases (hard and soft) will have distinct anisotropy fields and interact with each other via exchange and/or dipolar coupling. Additionally, even within a single phase, dipolar interactions between nanoparticles within the carbon matrix can influence the effective anisotropy experienced by individual particles.

Figure 7a and Figure S3b show the TS curves at lower temperatures: 30 and 40 K. It can be seen that the peaks in the negative scan become more prominent, height wise, than those in the positive scan, a reversal linked to the dominance of interaction-driven magnetic freezing or surface spin disorder [38]. Closer inspection of the TS curves near zero field revealed further complexity: the switching valley split into two minima separated by a small peak (Subset Figure 7a and Figure S3b). This peak is offset from zero field, shifting leftward for positive scans and rightward for negative scans, a behavior indicative of competing magnetic phases with distinct coercivities. The depth asymmetry of the valleys further supports this interpretation, mirroring the "wasp-waisted" hysteresis loops observed in static M(H) measurements (Figure 4b).

To quantify the magnetic anisotropy and its evolution with temperature, the $\mu_0 H_{Keff}$ values were extracted from the TS data for both M-300 and M-350 samples. The behavior of $\mu_0 H_{Keff}$ with respect to the temperature is given in Figure 7b. Almost across the entire measured temperature range (25 to 320 K), the $\mu_0 H_{Keff}$ values for M-350 are consistently higher than those for M-300. This observation aligns with the slight difference in average size between the two samples (6.5 ± 1 nm for M-300 vs. 7.5 ± 1 nm for M-350, see section 2.1), as larger particles generally possess higher effective anisotropy due to increased magnetic volume. Furthermore, the higher synthesis temperature for M-350 may lead to subtle differences in phase distribution, crystallite quality, or interfacial coupling between the magnetic phases, which can impact the overall anisotropy. Moreover, despite some fluctuations, the overall trend of $\mu_0 H_{Keff}$ with temperature appears relatively constant, particularly at temperatures well below the primary blocking temperature regime (250–350 K) identified from M(T) curves. Additionally, while transverse susceptibility measurements reveal a relatively stable effective anisotropy field across the measured temperature range, the coercivity, however, follows a decreasing trend over the same interval. This may be attributed to the system's multiphase character and the significant influence of thermal activation on reversal processes. The effective anisotropy field obtained from TS reflects the intrinsic energy barriers for magnetic moment rotation, which remain largely preserved due to interactions between the hard and soft phases. In contrast, coercivity is governed not only by these barriers but also by the thermally assisted switching of smaller particles and soft magnetic components present in systems, like ours. As temperature rises, thermal fluctuations facilitate

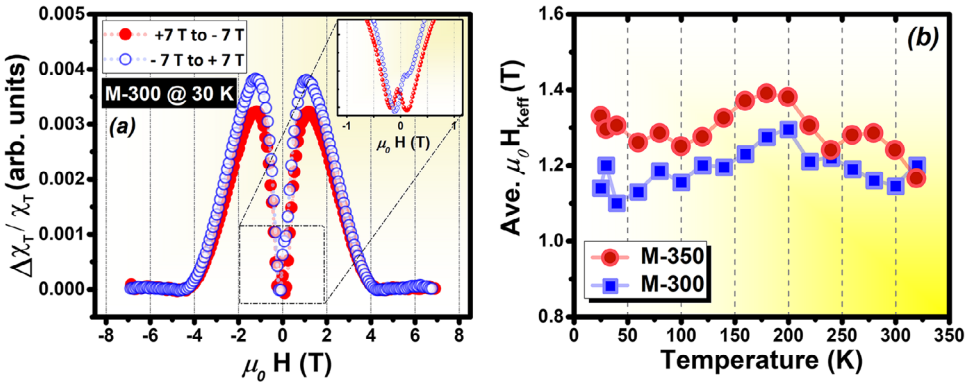

FIGURE 7 | (a) TS curve at 30 K of the M-300 sample with zoomed-in over the zero-field region (inset); (b) Evolution of the average $\mu_0 H_{\text{Keff}}$ with respect to temperature for both samples M-300 and M-350.

moment reversal in these components, thereby reducing the overall coercivity of the composite, even as the average anisotropy field remains stable. Therefore, the stability of $\mu_0 H_{\text{Keff}}$ in the face of a drop in coercivity serves as further evidence of a complex, collective magnetic behavior where the magnetic reversal is a thermally-activated, cooperative process of the present hard and soft magnetic phases. This detailed understanding of the dynamic and static magnetic behavior provides a more complete picture of the material's potential for frequency-dependent applications.

Overall, the TS spectra exhibit robust anisotropy peaks and a split switching singularity indicative of coexisting magnetic contributions and interparticle interactions. The near temperature-invariance and sample-dependent magnitude of $\mu_0 H_{\text{Keff}}$, together with the multi-component features, imply a distribution of effective anisotropies. In a random nanoparticle ensemble, such distributions map onto a spread of FMR conditions, broadening the magnetic-loss spectrum. As shown in the respective section, the FMR linewidths and large damping validate this picture. In combination with dielectric loss from the activated carbon host (which aids impedance matching), these magnetic signatures are consistent with broadband microwave absorption in magneto-dielectric composites.

2.3.2 | Ferromagnetic Resonance

Building on the discussion from transverse susceptibility measurements regarding the effective anisotropy and comparatively low-frequency (MHz) dynamic behavior, ferromagnetic resonance spectroscopy offers a powerful means to quantify the gyromagnetic ratio, effective magnetization, and damping behavior, thereby highlighting the dynamic magnetic response of the system under GHz excitation, a critical regime for applications in EMI shielding, radar systems and high-frequency devices (5G communications). FMR spectroscopy is a widely used technique to probe the dynamic response of a wide range of material systems (Ferro/ferrimagnetic materials as well as magnetic thin films, nanostructured systems and nanoparticles) under microwave excitation [53]. In nanoparticulate systems, FMR spectra typically exhibit broadened and asymmetric resonance line shapes due to inhomogeneities in size, anisotropy, and interparticle interactions [54]. Importantly, a broad resonance linewidth (ΔH) is proportional to the magnetic energy dissipation under microwave excitation, making it a key indicator of intrinsic microwave absorption capability. The theoretical foundation of FMR is captured by the Landau–Lifshitz–Gilbert (LLG) equation, which describes the precessional motion and damping of the magnetization vector $\boldsymbol{M}$ under an effective magnetic field. It can be expressed as [53]:

$$\frac{d\boldsymbol{M}}{dt} = -\mu_0\gamma\ (\boldsymbol{M}\times\boldsymbol{H}_{\text{eff}}) + \frac{\alpha}{M_s}\left[\boldsymbol{M}\times\frac{d\boldsymbol{M}}{dt}\right] \tag{5}$$

The above equation represents the precessional motion of the magnetization vector under an effective magnetic field. Ferromagnetic resonance occurs when the frequency of an applied microwave field matches this intrinsic precessional frequency. During this precession, intrinsic relaxation processes are quantified by the dimensionless Gilbert damping parameter, α. Analysis of the resonance field and linewidth enables extraction of key magnetic parameters such as the g-factor, α, and effective magnetization (M_{eff}) and anisotropy field (H_A), offering a microscopic picture of spin dynamics in the GHz regime.

For the measurement purposes, dried CFO@C nanoparticles of the respective samples were dispersed onto separate Magnesium Oxide (MgO) substrates using GE varnish and left to cure overnight under the influence of a neodymium magnet placed beneath the substrate to promote particle alignment and uniformity. MgO substrate was chosen due to its high dielectric strength and low microwave loss, minimizing background signal contributions during FMR measurements. The prepared sample-on-substrate was then placed inverted onto a coplanar waveguide (CPW), thereby sandwiching the nanoparticle layer between the CPW and the MgO substrate. A schematic of the experimental setup is shown in Figure 8a. FMR spectra were collected across a range of temperatures and frequencies, with excitation frequencies spanning from 18 to 30 GHz. The measurements were performed using a lock-in detection technique, in which the applied microwave field is amplitude-modulated, and the detected signal corresponds to the first derivative of a Lorentzian absorption line shape, rather than the absorption itself. At temperatures below 200 K, the signal-to-noise ratio dropped significantly, limiting reliable spectral analysis in that regime. Figure 8b and Figure S4a presents the frequency-dependent FMR spectra of the M-300, and M-350 samples recorded at 290 and 300 K, respectively. Figure 8c and Figure S4b, on the other

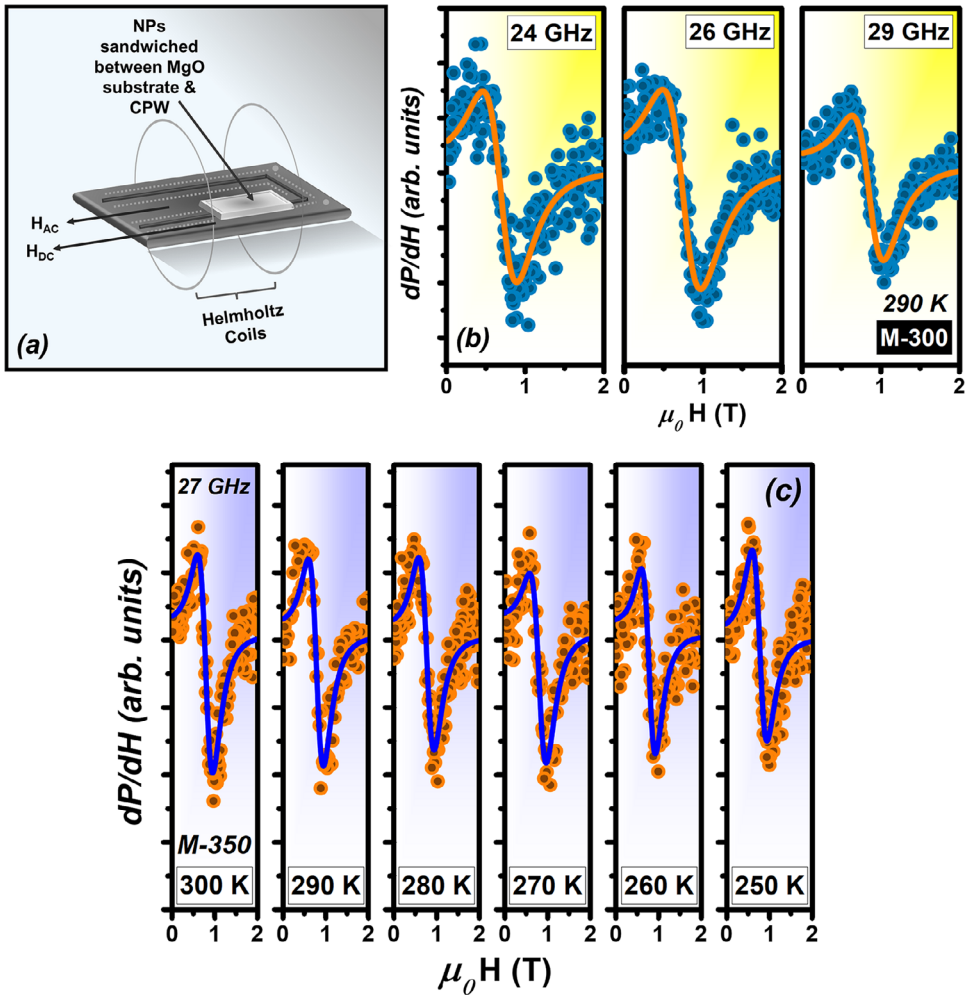

FIGURE 8 | (a) Schematic of the experimental geometry: CFO@C nanoparticles mounted on an MgO substrate and positioned on the coplanar waveguide (CPW). The Helmholtz coils apply a low-frequency modulation field (H_{AC}). A static bias field (H_{DC}) is applied along the sandwiched geometry (Substrate-NPs-CPW); (b) Fixed temperature FMR fitted spectra taken at different frequencies; (c) FMR spectra at 27 GHz of M-350 taken at different temperatures.

hand illustrate the FMR spectra of both samples at different temperatures corresponding to a single frequency of 27 and 26 GHz, respectively.

As can be seen, the FMR spectra exhibit broad, well-defined line shapes with large linewidths, as expected for magnetic nanoparticle assemblies [54]. While the theory of FMR is well established for isolated, single-domain particles, where resonance linewidths are relatively narrow and dominated by intrinsic damping with minimal extrinsic contributions, the interpretation becomes significantly more complex in real nanoparticle systems due to size distributions, multiphase contributions, and interparticle interactions [55]. In the case of our CFO@C nanocomposites, the observed line broadening may arise from several contributing factors: the distribution of particle size and the presence of multiple magnetic phases (CFO, Co-FCC, Co-HCP) introduce varied intrinsic anisotropies and resonance fields; random spatial orientation of nanoparticles within the carbon matrix further spreads the resonance condition; thermal fluctuations influence the magnetic moments of smaller particles; and magneto-dipolar interactions within the nanoparticle assembly alter the collective magnetic response [56, 57]. These effects act in concert leading to a distribution of resonance fields, thereby effectively smoothening and significantly broadening the FMR spectra observed in our experiments, a desirable feature for broadband EM wave absorbers [54, 58].

To quantitatively analyze the FMR line shapes, we employed a model based on the linear combination of symmetric and antisymmetric derivatives of Lorentzian functions, as described by the following relation [59, 60].

$$dP/dH = \left(\frac{\Delta H/2 \times (H_{DC} - H_{res})}{\left((H_{DC} - H_{res})^2 + (\Delta H/2)^2 \right)^2} \right) P_s + \left(\frac{(\Delta H/2)^2 - (H_{DC} - H_{res})^2}{\left((H_{DC} - H_{res})^2 + (\Delta H/2)^2 \right)^2} \right) P_A + P_0 \quad (6)$$

In this expression, $\frac{dP}{dH}$ is the measured lock-in detected signal as a function of the applied static magnetic field H_{DC}, H_{res} denotes

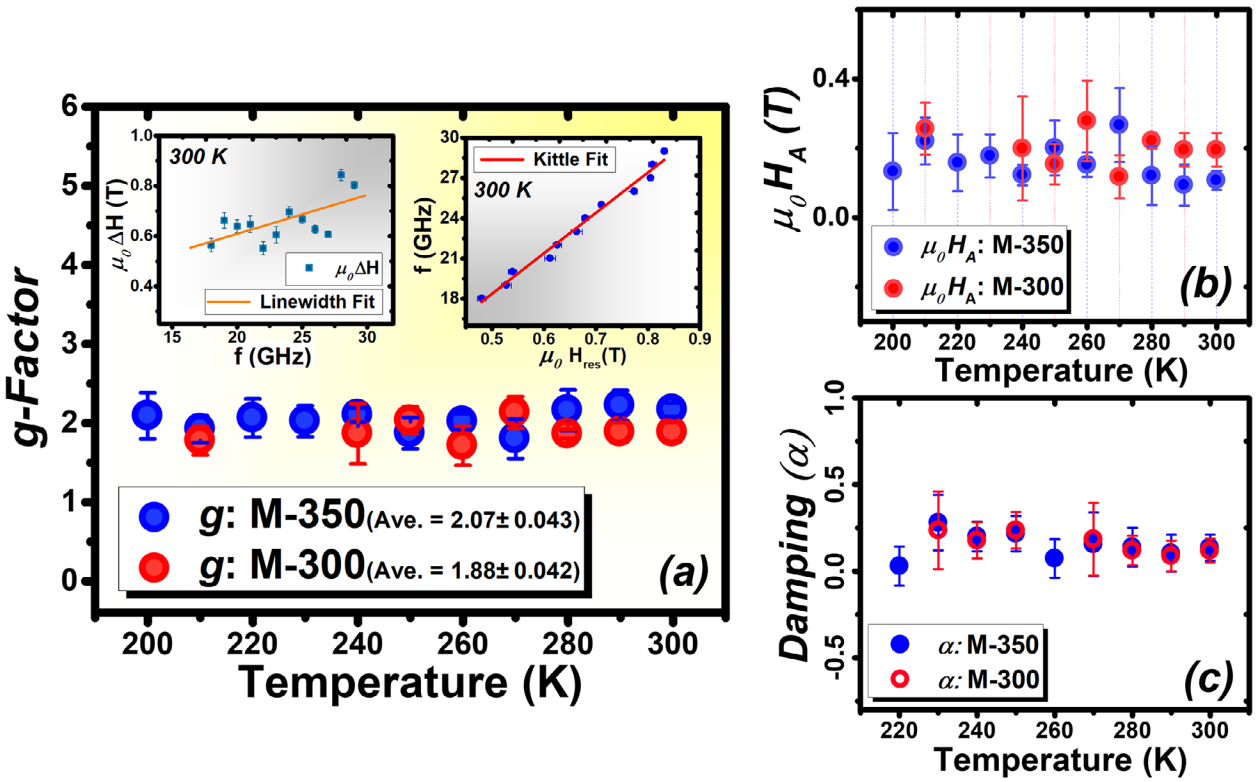

FIGURE 9 | (a) Behavior of the Landé *g*-factor with respect to temperature for M-300 and M-350 samples. Insets: top left—linear fit of linewidth vs. frequency for damping extraction; top right—representative Kittel fit used to determine *g*-factor and anisotropy field (H_A). Behavior of (b) Anisotropy field (H_A) and (c) Gilbert damping (α) with temperature.

the resonance field, and ΔH represents the linewidth parameter of the derivative signal. The coefficients P_s and P_A correspond to the amplitudes of the symmetric and antisymmetric components, respectively, while P_0 is a constant offset parameter accounting for baseline shifts. The solid lines superimposed on the data points in Figure 8b,c and Figure S4a,b illustrate the resulting fits, which accurately capture the experimental line shapes across the frequency and temperature range studied.

The extracted resonance field values at different excitation frequencies were used to construct frequency (f) vs. resonance field (H_{res}) relationships. As the magnetic nanoparticles in the carbon matrix are dilute and quasi-spherical in shape, that is why the f vs. H_{res} curves were analyzed using the Kittel equation for spherical particles (Equation 7). For comparison purposes, the corresponding analysis using the in-plane model of the Kittel equation is provided in the Figure S4c [61, 62].

$$f = (\gamma/2\pi)\ (H_{res} + H_A) \tag{7}$$

In the above equation, γ is the gyromagnetic ratio, defined as $\gamma = g\mu_B/\hbar$, where g is the Landé g-factor; μ_B is the Bohr magneton, and H_A represents the anisotropy field. A representative fit using the above equation is shown in top right inset of Figure 9a. From the slope, we estimated the value of γ, which was subsequently used to determine the *g*-factor, while the intercept provided an estimate of the H_A.

Furthermore, to determine the intrinsic damping parameter and quantify the various contributions, the ΔH obtained from the fittings of the line shapes was plotted as a function of frequency. This dependence was then fitted with a linear equation as follows:

$$\Delta H = \Delta H_0 + (4\pi a/\gamma\mu_0)\, f \tag{8}$$

In the above expression, ΔH_0 indicates the frequency-independent contribution to the linewidth, also termed inhomogeneous broadening. The slope yields the Gilbert damping, α. A representative linear fit used to extract the aforementioned parameter is provided in the top right of Figure 9a.

For both M-300 and M-350 samples, the *g*-factor remains largely constant across the measured temperature range (200 to 300 K), as shown in Figure 9a. This temperature independence is commonly observed in ferrimagnetic systems below their Curie temperature, where the dominant electronic configurations and spin-orbit coupling remain stable once the long-range magnetic order is established [63]. The g-factor is an intrinsic parameter of the material reflecting the ratio of spin angular momentum to orbital angular momentum, primarily determined by the electronic structure and local environment of the magnetic ions. Once the nanoparticles are magnetically blocked (which is the case over most of our FMR temperature range: 200–300 K), the fundamental electronic configurations and spin-orbit coupling that govern the g-factor do not undergo significant changes with temperature. This consistency further validates the stability of the magnetic phases and their interactions across this thermal range, similar to what we have observed in our previous Co-

CFO nanocomposite, where we acquired a $g_{ave} = 1.89$ [26]. The estimated g-factor for M-300 is 1.88 ± 0.04, whereas for M-350, it is 2.07 ± 0.04. This highlights how sensitive the g-factor is to subtle changes in the material's composition, phase distribution, and interfacial characteristics, which are inherently influenced by the specific synthesis route and processing temperatures [64]. The inclusion of the carbon matrix and the slightly different synthesis conditions in the CFO@C system likely modify the degree of metallic Co formation, its interaction with the CFO phase, and the cation distribution within the ferrite, leading to these distinct effective g-factors.

The anisotropy field, H_A for both the samples estimated by considering the spherical Kittel model, is shown in Figure 9b. As can be seen, H_A exhibits an essentially temperature-independent trend that closely mirrors the near-constant behavior of $\mu_0 H_{keff}$ obtained from the TS measurements. However, the absolute magnitude of H_A from FMR is systematically lower than those estimated from the respective TS analysis. This difference may be attributed to the distinct sample preparations and measurement geometries: the TS measurements were performed on tightly packed powder in a gelatin capsule (high local particle density), whereas the FMR samples were prepared as a more diluted, magnetically aligned nanoparticle layer on the MgO/CPW. Denser packing increases interparticle dipolar (and, where present, interparticle exchange) interactions and thereby enhances the quasi-static effective anisotropy sensed in TS [65]. In contrast, the dilute, aligned FMR sample has relatively larger average interparticle separations and a preferential orientation, reducing the contribution of collective dipolar fields to the resonance condition. Simple dipolar-field estimates (Supporting Information) show that changing mean center-to-center spacing from a few nanometers to ∼ 10 nm significantly alters local dipolar fields (Figure S5c), consistent with the observed differences between TS and FMR. It is also important to note that TS measurements (typically in MHz range) and FMR measurements (in GHz range) probe magnetization dynamics at different frequency regimes. While TS measurements probe the linear dynamic magnetic response of the system at lower frequencies, FMR is directly sensitive to the resonance conditions at much higher frequencies. Thus, while fundamentally linked, the specific manifestations of anisotropy in these two measurements can vary. Nonetheless, the overall temperature independent trend of H_A closely tracks that of $\mu_0 H_{keff}$ from the TS measurements highlighting the stability of the anisotropy in the CFO@C nanocomposites.

Figure 9c shows that the Gilbert damping estimated from the linewidth–frequency analysis remains high ($\alpha_{average} \approx 0.14 \pm 0.0012$) and essentially temperature independent over the 200–300 K range. Such behavior suggests that the dominant relaxation channels are not primarily governed by thermally activated magnon–phonon relaxations, which typically introduce a noticeable temperature dependence, but are instead predominantly controlled by intrinsic electronic and interfacial scattering mechanisms [66, 67]. This temperature invariance thus provides a critical constraint on the microscopic origin of the damping and points toward mechanisms rooted in spin–orbit coupling, structural disorder, and interfacial exchange rather than thermally driven relaxation. Furthermore, from an application perspective, this thermal stability ensures that the magnetic dissipation and absorption characteristics remain consistent across typical operating environments. Such performance reliability at and around room temperature is a significant advantage for the practical implementation of these nanocomposites.

A primary intrinsic contribution to the large damping originates from the cobalt ferrite phase itself. In spinel CFO, Co^{2+} ions occupying octahedral sites possess a partially unquenched orbital moment, leading to strong spin–orbit coupling. Microscopically, this coupling provides an efficient channel for transferring angular momentum from the precessing spin system to the lattice via spin–orbit–mediated electron–phonon interactions. As a result, the coherent precession of the magnetization decays rapidly, manifested as enhanced Gilbert damping. This mechanism is well established in cobalt-containing ferrites as well as other ferrite systems, and is consistent with the high damping observed in our system [67–70]. To place the magnitude of the extracted damping and related FMR parameters in a broader materials context, a comparative summary of representative systems reported in the literature is provided in Table S3, including particle size, frequency range, gyromagnetic ratio, anisotropy field, g-factor, and Gilbert damping.

Further insight into the role of spin–orbit coupling can be obtained from the effective g-factor extracted from the FMR analysis. In crystal-field-based descriptions of transition-metal ions, deviations of the g-factor from the free-electron value ($g \approx 2.0023$), reflect the influence of spin–orbit coupling and orbital contributions to the magnetic moment. This behavior is commonly captured in perturbative models through relations of the form: $g = 2[1 - (\frac{\lambda}{\Delta})]$, where λ denotes the spin–orbit coupling constant and Δ the crystal-field splitting energy [67]. While such expressions are rigorously applicable to single-ion systems with well-defined electronic environments, the g-factors measured here represent effective values averaged over exchange-coupled magnetic phases and interfacial regions within the CFO@C nanocomposite. Consequently, a quantitative extraction of λ is not attempted. Nevertheless, the deviation of g from the free-electron value in both samples qualitatively supports the presence of significant spin–orbit-mediated relaxation channels, consistent with the enhanced Gilbert damping observed in this system.

In addition to spin–orbit–mediated lattice coupling, electronic relaxation processes intrinsic to nanoscale spinel ferrites may further contribute to the large damping observed here [71]. In CFO, mixed-valence configurations such as Fe^{2+}/Fe^{3+} and Co^{2+}/Co^{3+} can be stabilized by defects, surface disorder, and interfacial environments, particularly in nanostructured composites. Rapid electron hopping between neighboring octahedral cations generates time-dependent local exchange fields that efficiently couple to the uniform precessional mode probed in FMR, providing an additional channel for angular momentum dissipation [72]. Because these electronic fluctuations occur on timescales compared to the precession period, they contribute to linewidth broadening in a manner that is largely insensitive to moderate temperature variations, consistent with the experimentally observed temperature-independent damping [70].

Beyond intrinsic contributions, extrinsic relaxation mechanisms associated with the multiphase nature of the nanocomposite are expected to play a substantial role [73, 74]. The coexistence of magnetically hard CFO and softer metallic Co phases, as revealed by

the XRD, hysteresis-loop deconvolution and transverse susceptibility measurements, creates nanoscale magnetic inhomogeneity and sharp interfacial exchange gradients. Microscopically, such interfaces break the translational symmetry of the magnetic system, allowing the uniform precessional modes probed in FMR to couple to degenerate or nearly degenerate spin-wave modes. This mode conversion, often described phenomenologically as two-magnon or interfacial scattering, leads to an effective transfer of energy from coherent precession into incoherent magnon excitations, thereby broadening the resonance linewidth and enhancing the damping [70].

Nanoscale confinement further amplifies these relaxation pathways. The high surface-to-volume ratio of the nanoparticles introduces surface spin disorder arising from broken exchange bonds, local strain, and reduced coordination at the particle boundaries. These disordered surface spins experience a distribution of local anisotropy fields and relaxation rates, acting as efficient sinks for angular momentum and facilitating additional magnon scattering [75, 76]. In addition, the surrounding carbon matrix, while primarily serving as a structural scaffold, modifies the magnetic boundary conditions at the particle surface. By electronically isolating nanoparticles while simultaneously introducing interfacial electronic states and conductive pathways, the carbon environment may influence spin relaxation through enhanced spin dephasing or interfacial spin-flip processes, further contributing to the overall damping [50, 77, 78].

Collectively, these intrinsic and extrinsic mechanisms form a hierarchical damping spectrum in the CFO@C nanocomposite, dominated by strong spin–orbit coupling in the ferrite phase and reinforced by interfacial exchange scattering and nanoscale disorder. While a quantitative separation of individual damping contributions would require complementary measurements such as angular-dependent FMR or systematic interface engineering, the consistency between the observed temperature stability, multiphase magnetic structure, and broad FMR linewidths supports this mechanistic interpretation. Importantly, this combination of damping channels highlights the robust microwave loss behavior of the composite and underscores the role of multiphase and interfacial design for high performance microwave absorption devices.

2.3.3 | Magnetic Hyperthermia

To complement the high-frequency dynamic analyses, magnetic hyperthermia experiments were conducted to evaluate the low-frequency heating efficiency of the CFO@C nanocomposites. Building on the insights from the preceding sections, we estimate the magnetic hyperthermia efficiency of the nanocomposites through field-dependent magnetization, specific absorption rate (SAR) and intrinsic loss power analyses. Magnetic hyperthermia relies on energy dissipation from magnetic nanoparticles under an alternating magnetic field (AMF), a process dependent on their magnetic properties at physiological temperatures. As shown in Figure 10b, the magnetization vs. field curve measured at 300 K exhibits a finite coercivity (~ 33 mT), indicating that still some nanoparticles remain in a blocked state at room temperature consistent with that already discussed in Section 2.2. Such non-vanishing coercivity is expected for hard ferrite systems below their blocking temperature, where thermal energy is insufficient to overcome the anisotropy barrier, resulting in stable magnetization reversal dynamics [79]. In these kinds of systems, the heat dissipation efficiency, often quantified via the specific absorption rate, is expected to scale with the amplitude of the applied magnetic field.

The magnetic heating efficiency of the CFO@C nanocomposites was assessed through self-heating characteristic curves obtained under AMF using an induction heating system as already discussed in the experimental section of this work. To ensure proper experimental control, the glass vial containing the nanoparticle suspension was positioned at the center of the coil using a Styrofoam disc to maintain geometric alignment and thermal equilibrium. Additionally, the inner walls of the coil were lined with silicon paper to thermally insulate the sample from direct heating caused by the coil itself. A schematic view of the experimental setup is provided in Figure 10a. For these measurements, AMF amplitudes of 400, 600, and 800 Oe were applied at a fixed frequency of 310 kHz for a duration of 15 min. To evaluate the impact of dispersion environment and concentration, two distinct nanoparticle concentrations (0.5 and 1 mg/mL) were prepared and tested in both D. I. water and agar media. The self-heating characteristics under AMF are illustrated by the time-dependent temperature profiles shown in Figure 10c,d and Figure S7a,b for suspensions in DI water and agar, respectively. A designated hyperthermia threshold, defined as the 40°C–45°C temperature interval is included as a dashed band for reference. Analysis of these heating curves reveals that under an AMF of 800 Oe, the agar-based suspensions consistently achieve this therapeutic threshold more rapidly than their DI water counterparts.

The conversion of magnetic energy into thermal energy by magnetic nanoparticles subjected to an alternating magnetic field is commonly quantified using the SAR. For the current study, SAR was determined calorimetrically through two main approaches. The first assumes adiabatic conditions and uses the initial slope method, which estimates SAR from the initial linear portion of the early-time heating curve. The second accounts for non-adiabatic heat losses and includes both the Newton cooling model and the Box–Lucas fitting approach. While Newton's law of cooling is a fundamental physical model describing heat loss to the surroundings, the Box–Lucas equation is an empirical fitting function derived from it and widely used for practical modeling of experimental heating curves under realistic (non-ideal) conditions [80].

In the initial slope method, SAR is calculated under the assumption that heat losses to the environment are negligible during the early phase of heating, effectively approximating adiabatic conditions. This assumption holds over a short time window, where the temperature vs. time profile remains approximately linear. In the current work, a time interval of 120 s was selected based on the linearity of the heating curve within that duration. SAR was then calculated using the relation:

$$\mathrm{SAR} = (\mathrm{Slope})_i . [C/m] \quad (9)$$

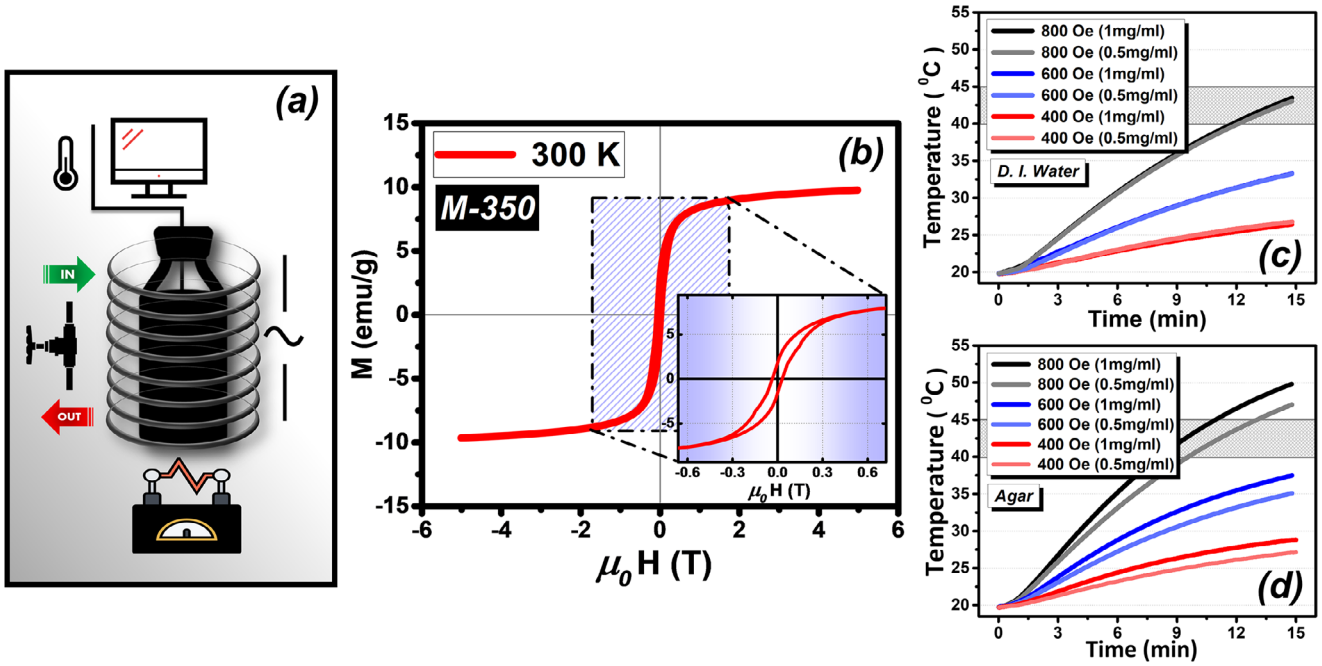

FIGURE 10 | (a) Schematic illustration of the magnetic hyperthermia experimental setup. (b) Room-temperature magnetization vs. field (M–H) curve for the M-350 sample, showing finite coercivity (inset: zoomed-in view near the origin). (c,d) Self-heating characteristic curves of CFO@C nanocomposites recorded at two concentrations (0.5 and 1.0 mg/mL) under alternating magnetic fields of 400, 600, and 800 Oe at 310 kHz, in DI water and agar media.

where $(\text{Slope})_i$ is the slope of the temperature rise during the linear region expressed as $\frac{\Delta T}{\Delta t}$, C is the specific heat capacity of the dispersion medium, and m is the mass concentration of sample in the dispersion medium. The analysis of the SAR consistently demonstrated a direct proportionality between SAR values and the applied AMF amplitude across all investigated media and concentrations (Figure S7c,d). Notably, samples with a concentration of 1 mg/mL consistently showed lower SAR values compared to those at 0.5 mg/mL. This inverse trend in heating efficiency with increasing concentration is typically attributed to nanoparticle aggregation at higher concentrations [81]. For hard magnetic materials like CFO, such aggregation reduces the overall magnetic relaxation efficiency, thereby diminishing the system's heating capability.

To quantify SAR beyond the initial heating phase, it is important to account for heat dissipation to the surroundings, as the observed temperature profiles often exhibit a non-linear increase with time under the applied alternating magnetic field. While the initial slope method provides a direct measure of heat generation under adiabatic assumptions (valid only for the very early stages of heating), it does not account for the continuous heat loss that occurs as the suspension temperature rises [82]. Therefore, to obtain a comprehensive estimation of SAR across the entire heating curve, we employed non-adiabatic fitting approaches, specifically the Box-Lucas equation and a model based on Newton's Law of Cooling, to analyze the full time-dependent temperature data (Figure 11 and Figure S7e,f). Both these models incorporate heat exchange with the surrounding medium over extended time intervals [41]. Additionally, it is important to mention that although these models may not fully capture nanoscale heat transfer physics, they serve as robust tools to approximate SAR under more realistic (lossy) conditions. Thus, by applying multiple fitting approaches, we aim to offer a comparative picture of heating performance that reflects both early and long-term energy dissipation behavior in the CFO@C system. To account for thermal losses to the surrounding environment and capture the full time-dependent heating behavior, the experimental heating curves data was fitted using the Box–Lucas model as follows:

$$T\ (t) = A\left(1 - e^{-B(t-t_0)}\right) \tag{10}$$

where A and B are the parameters that were estimated from the fitting of the heating curves using the above expression. These parameters were then placed in the equation below to extract SAR.

$$\text{SAR} = \frac{\text{C.A.B}}{\text{m}} \tag{11}$$

where C is the specific heat capacity of the dispersion medium and m is the mass concentration of the suspended sample.

As already mentioned, under non-adiabatic conditions, the temperature evolution of a nanoparticle suspension exposed to an alternating magnetic field can also be modeled using the Newton cooling law. The time-dependent temperature profile is described by the equation

$$T\ (t) = T_0 + \Delta T_{\max}\left(1 - e^{-\frac{t}{\tau}}\right) \tag{12}$$

where T_0 is the initial temperature, $\Delta T_{\max}$ represents the maximum temperature rise, and τ is the characteristic time constant. The extracted parameters $\Delta T_{\max}$ and τ are used to calculate the

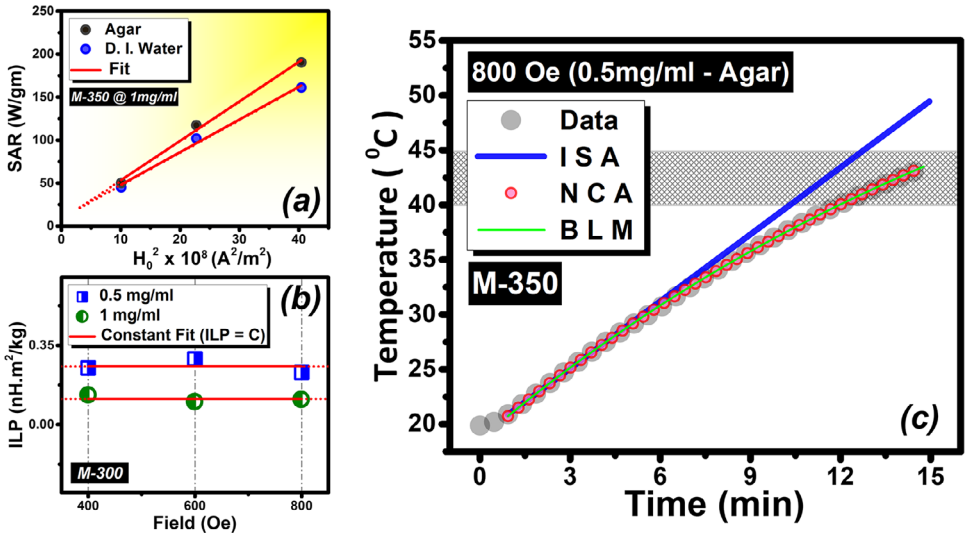

FIGURE 11 | Magnetic hyperthermia analysis of CFO@C nanoparticles: (a) Linear fit of specific absorption rate (SAR) as a function of $H_0{}^2$, validating the quadratic dependence predicted by the Linear Response Theory (LRT); (b) Constant fit of intrinsic loss power ($SAR/fH_0{}^2$) across applied field strengths, confirming system stability and LRT applicability; (c) Experimental heating curves of sample M-350 under alternating magnetic field, fitted using three different methods: Initial Slope Approach (ISA), Newton Cooling Approach (NCA), and Box-Lucas method (BLM).

SAR as follows:

$$\mathrm{SAR} = \frac{\mathrm{C}}{\mathrm{m}} \cdot \frac{\Delta T_{\max}}{\tau} \tag{13}$$

where C is the specific heat capacity of the dispersion medium, and m is the mass concentration of the sample. The SAR values obtained from all three approaches are provided in Table 1 and Table S4. The SAR values derived from the non-adiabatic models are typically found to be higher than those obtained from the initial slope method, a phenomenon consistently reported in the literature for various magnetic ferrite based nanoparticle systems, as non-adiabatic models take into account the temperature evolution over an extended time scale where heat loss becomes significant [41, 83]. Additionally, while the non-adiabatic approaches share the same mathematical form, that is, saturating exponential, they differ in their physical basis and interpretation. The Newton cooling model is grounded in heat balance framework. Its parameters, maximum temperature rise ($\Delta T_{\max}$) and characteristic time constant (τ), carry direct physical meaning related to the system's thermal properties. In contrast, the Box–Lucas model is employed as a phenomenological fitting function: its coefficients A and B map numerically onto $\Delta T_{\max}$ and $1/\tau$, but are typically used in practice as empirical fitting parameters without invoking the underlying thermal assumptions. Despite their mathematical similarity, using both models provides complementary insights: the Newton model offers a physically interpretable framework, while the Box–Lucas model serves as a flexible empirical tool for comparing heating dynamics across samples. By applying both, we ensure robustness in our SAR estimation under realistic, non-adiabatic conditions.

While the SAR values extracted using various fitting methods offer quantitative insight into the heating performance, understanding the underlying physical mechanisms responsible for heat generation is essential for interpreting these results. In magnetic nanoparticle systems subjected to AMF, thermal energy dissipation typically arises from a combination of loss mechanisms, including magnetic hysteresis, eddy current losses, and relaxation processes (Brownian and Néel relaxation). The relative contribution of each mechanism depends on factors such as particle size, magnetic anisotropy, aggregation state, and matrix confinement. Given the finite coercivity observed at 300 K (as shown in Figure 10b), magnetic hysteresis losses are likely playing a non-negligible role in our CFO@C system. While the smaller nanoparticles ($<$ 9 nm) enter a superparamagnetic regime at this temperature (Figure 2), the finite coercivity may arise from the subset of larger particles ($>$ 9 – 10 nm) that remain magnetically blocked. In this case, hysteresis losses (though relatively small) may arise from the repeated magnetization reversal of the blocked particles in response to the alternating field, dissipating energy corresponding to the area of the hysteresis loop and is characteristic of magnetically hard phases like cobalt ferrite [84]. Additionally, due to the nanoscale size regime of our particles system, both Néel relaxation and Brownian relaxations are expected to be active. Néel relaxation involves the rotation of the magnetic moment within the particle, while Brownian relaxation involves the statistical physical rotation of the particles within the dispersion media. The impact of particle aggregation, especially at higher concentrations, would directly influence and restrict this Brownian contribution, as previously discussed. In contrast, eddy current losses may be considered negligible for our system. Such losses require significant electrical conductivity to support circulating currents. However, cobalt ferrite is insulating, and the carbon matrix is only weakly conducting, so the effective resistivity of the composite is high. Consequently, appreciable eddy currents cannot form. Moreover, at the employed frequency of 310 kHz and with nanoparticles of only $\sim$ 8 nm, the particle dimensions are far below the electromagnetic skin depth, further suppressing any residual eddy current effects; even with the presence of metallic cobalt phases or potentially carbon matrix, the porous and discontinuous nature of the activated carbon further limits large-scale eddy current formation. Therefore, the heating behavior in the CFO@C system is governed by a

TABLE 1 | Comparison of SAR values acquired from the fits by employing different approaches.

M-300 SAR comparison (W/g)												
	Initial slope method				Newton cooling approach				Box–Lucas approach			
	D.I. water		Agar		D.I. water		Agar		D.I. water		Agar	
Field (Oe)	0.5 mg/mL	1 mg/mL	0.5 mg/mL	1 mg/mL	0.5 mg/mL	1 mg/mL	0.5 mg/mL	1 mg/mL	0.5 mg/mL	1 mg/mL	0.5 mg/mL	1 mg/mL
400	80.1	41.4	78.4	54.6	109.4	45.5	91.6	66.4	265.2	106.8	220.5	153.5
600	166.7	75.9	184.8	101.5	213.1	97.4	208.3	132.2	365.5	165.3	382.0	217.1
800	292.1	143.1	303.8	185.5	370.8	187.9	322.8	230.6	519.7	259.7	446.3	310.1

combination of relaxation and hysteresis losses, modulated by the key parameters (like, particle size, coercivity, and magnetic anisotropy) inherent to the multiphase nanostructure.

Given the abovementioned observations and since our nanoparticles lie in the sub 10 nm size range, near the superparamagnetic–blocked boundary, we assessed the applicability of the Linear Response Theory (LRT) to our system. LRT is generally valid when the magnetic field amplitude (H_0) is small compared to the magnetic anisotropy field ($\mu_0 H_K$), and when energy dissipation arises primarily through linear relaxational processes such as Néel and Brownian relaxation [85, 86]. In our case, the applied field amplitudes (400–800 Oe) are below the expected $\mu_0 H_K$ values for cobalt ferrite (also shown in Figure 7b in our TS analysis section), and the operating frequency (310 kHz) falls within a regime where the relaxation mechanisms are expected to dominate [85]. While our system exhibits finite coercivity, indicating the presence of magnetic hysteresis losses, we apply LRT to primarily probe the contribution and scaling behavior of the relaxational component to the overall heating dynamics. Under LRT, the SAR is predicted to scale quadratically with the applied magnetic field, as described by the relation:

$$SAR = {\mu_0}^2 {M_s}^2 V {H_0}^2 (2\pi f \tau_R)^2 / 3K_B T \tau_R \rho \left[1 + (2\pi f \tau_R)^2\right] \quad (14)$$

where μ_0 is the vacuum permeability, M_s is saturation magnetization, V is the particle volume, H_0 is the magnetic field amplitude and τ_R is the relaxation time. To evaluate the applicability of this model under our experimental conditions, we note that in our case the frequency is fixed at 310 kHz while the magnetic field amplitude H_0 is varied. This allows the LRT expression to simplify a quadratic dependence of SAR on H_0, that is,

$$SAR \propto {H_0}^2 \quad (15)$$

The above given proportionality serves as an experimental litmus test for the validity of LRT in nanoparticle hyperthermia systems. Figure 11a shows the plot of SAR values, calculated using the initial slope method, as a function of ${H_0}^2$. As can be seen, the data displays a linear trend, consistent with the theoretical prediction. To further quantify this, we applied a linear fit (indicated by the red line in Figure 11a), which captures the trend well and passes close through the origin, suggesting that our experimental SAR scales as ${H_0}^2$, as expected in the LRT regime. This observation suggests that the heating mechanism under our conditions is predominantly driven by the linear relaxation dynamics.

To further assess the heating efficiency of our CFO@C system in a field- and frequency-independent manner, we evaluated the Intrinsic Loss Power (ILP), a widely used figure of merit in magnetic hyperthermia studies. ILP is defined as:

$$ILP = \frac{SAR}{f.{H_0}^2} \quad (16)$$

where SAR is the specific absorption rate, f is the frequency of the alternating magnetic field (kHz), and H_0 is the amplitude of the applied magnetic field. This normalization removes the dependence of SAR on experimental conditions, allowing for a more meaningful evaluation of the intrinsic heating capability of the nanoparticles themselves [85]. In our case, the ILP values

were calculated using SAR values obtained via the initial slope approach already discussed. The acquired results as a function of magnetic field amplitude are presented in Figure 11b. As evident from the figure, the ILP values remain nearly constant across the tested field range. For the 0.5 mg/mL dispersion for both the samples, the ILP values fall within the magnetic field range of $0.2 - 3.1\,\mathrm{nH \cdot m^2/kg}$ in both samples, which is comparable to those reported for commercially available ferrite nanoparticles system, highlighting the efficient heating performance of our CFO@C nanocomposites [85]. To place the heating efficiency of the present CFO@C nanocomposites in context, Table 2 summarizes a quantitative comparison of SAR and ILP values reported for representative carbon-containing and cobalt ferrite–based nanocomposite systems under comparable conditions.

In addition, and with the aim to validate the field independence of ILP predicted by LRT, we plotted the ILP values as a function of the applied magnetic field strength and then performed constant fit over the data points. As expected, the ILP does not exhibit any significant dependence on H_0, consistent with the theoretical assumption that SAR scales as ${H_0}^2$ under LRT, making ILP a field-invariant quantity. The constant fit captures the ILP data well, yielding a fitted value with a small standard error (as shown in Figure 11b) that closely matches the average of the measured ILP values across the full magnetic range. This tight clustering and lack of deviation from the constant trend confirm that the heating efficiency, when normalized to magnetic field and frequency, remains stable, further supporting the applicability of LRT to our system under the tested conditions. The latter suggests that while the heating behavior in the CFO@C system is governed by a combination of relaxation and hysteresis losses, it is predominantly driven by linear relaxation dynamics, thereby reinforcing the observed operation within the LRT regime inferred from the *SAR vs* ${H_0}^2$ analysis.

Overall, while the hyperthermia analysis establishes relaxation-dominated magnetic losses in the kHz regime and confirms operation within the LRT framework, the CFO@C system has been interrogated across a much broader frequency spectrum in this work. When considered together with the transverse susceptibility and ferromagnetic resonance measurements, these results enable a comprehensive assessment of how magnetic energy dissipation evolves from low-frequency relaxation processes to high-frequency precessional dynamics. Therefore, to fully appreciate the multifunctionality of this system beyond the regime-specific analyses presented above, it is instructive to place the observed magnetic loss behavior of the CFO@C nanocomposites within a broader frequency-dependent framework spanning kHz to GHz. At microwave frequencies, magnetic energy dissipation is governed primarily by precessional dynamics, where the Gilbert damping reflects the efficiency of angular momentum transfer from the spin system to the lattice. The relatively high and temperature-stable damping observed here ($\alpha \approx 0.14$ over 200–300 K) suggests that magnetic losses are dominated by intrinsic and interfacial mechanisms that are largely insensitive to moderate thermal fluctuations [66, 67]. These include strong spin–orbit coupling in the cobalt ferrite phase, interfacial exchange scattering arising from the coexistence of hard (CFO) and soft (metallic Co) magnetic phases, and enhanced magnon scattering associated with nanoscale disorder and surface effects, as discussed in detail in the FMR analysis [68–76]. The weak

TABLE 2 | Comparison of magnetic hyperthermia performance, expressed in terms of SAR and ILP, for representative carbon-containing and cobalt ferrite–Based nanocomposite systems reported in the literature. Experimental conditions, including field amplitude, frequency and concentration, are included where available.

NCs/NPs (Type)	Morphology	Size/Domain (nm)	Frequency (kHz)	Field	Concent. $\left(\frac{\mathrm{mg}}{\mathrm{mL}}\right)$	SAR $\left(\frac{\mathrm{W}}{\mathrm{g}}\right)$	ILP $\left(\frac{\mathrm{nHm^2}}{\mathrm{kg}}\right)$	Refs.
$Mn_{0.5}Zn_{0.5}Fe_2O_4$/MWCNTs	Interwoven/Complex	80 – 120	238–380	6.6 kA/m	5–20	20–140	—	[87]
Ni@C	Composite	10 – 50	310	400–800 Oe	0.5–1	75–375	0.2–0.46	[24]
Fe_3O_4/*MWCNTs*	Spherical/Tubular	32 – 35	336	10–15 kA/m	1	175–974	3–8	[88]
MWCNT/$CoFe_2O_4$	Composite	27 – 38	336	8–23 kA/m	1	30–259	0.9–2.3	[89]
Co – $CoFe_2O_4$	Composite	50	310	800 Oe	0.5	275	0.2	[26]
Fe_3O_4/$CoFe_2O_4$	C@S	6.35 – 8.8	300	100 Oe	50	5–15	0.75	[90]
SPIONs@C	C@S/composites	10 – 40	150	10–30 kA/m	2	10–450	—	[91]
$CoFe_2O_4$@C	Cluster	150 – 250	765	0.025–0.03T	0.5–2	52–241	—	[92]
FeCo@Graphite/C	Irregular/Complex	42–104	300	325 Oe	5	68–191	0.95	[93]
$CoFe_2O_4$	Cubic	15	252	15.89 kA/m	6	53.4	0.84	[94]

temperature dependence of α further suggests that these loss channels are robust against thermal fluctuations in this range, a desirable characteristic for broadband and thermally stable microwave absorption.

At intermediate (MHz) frequencies, as probed by transverse susceptibility measurements, the dynamic response transitions from precessional to quasi-linear magnetization processes, where effective magnetic permeability and anisotropy dominate the loss behavior. In this regime, the coexistence of hard and soft magnetic phases leads to a spectrally broadened distribution of switching fields and relaxation times, enhancing magnetic losses over an extended frequency window. The Voigt-profile deconvolution of the hysteresis loops quantitatively demonstrates how these magnetically distinct phases contribute separately yet in a complementary manner to the overall permeability spectrum.

Last, at low frequencies (kHz), relevant to magnetic hyperthermia, magnetic losses arise predominantly from Néel and Brownian relaxation processes rather than coherent spin precession. Consistent with LRT, the observed heating efficiency under physiologically relevant field amplitudes reflects relaxation-controlled energy dissipation governed by particle size, anisotropy barriers, and thermal activation. Importantly, the same multiphase design that enhances high-frequency damping also broadens the relaxation spectrum at low frequencies, enabling efficient dissipation without relying much on hysteretic losses.

These results reveal that carbon-confined CFO@C nanocomposites dissipate magnetic energy through distinct yet complementary mechanisms across kHz, MHz, and GHz regimes. The multiphase magnetic architecture primarily tunes magnetic permeability and damping over a wide frequency range, whereas the conductive carbon matrix provides dielectric loss pathways and promotes impedance matching. This hierarchical loss mechanism highlights the material's capability for broadband electromagnetic attenuation and multifunctional performance across disparate application-relevant frequency domains.

3 | Conclusion

In this work, the synthesis and systematic characterization of two distinct cobalt ferrite-based nanoparticle samples embedded within a porous activated carbon matrix (CFO@C) is presented. We have successfully demonstrated that the composite architecture, incorporating a multiphase magnetic component (cobalt ferrite with minor elemental Co-rich phases) within the carbon matrix, establishes a compelling platform for achieving tunable static and dynamic magnetic behavior across an expansive frequency spectrum, from kHz to GHz.

Magnetization as a function of temperature and applied magnetic field evidence room-temperature magnetic blocking, finite coercivity, and a temperature dependence of saturation magnetization described by Bloch's law. The obtained Bloch exponents are in good agreement with values reported for similar nanoparticle systems. Kneller law analysis of the temperature-dependent coercivity data gives blocking temperatures consistent with magnetization vs temperature measurements, and yielding suppressed Kneller exponents, indicative of complex reversal mechanisms beyond ideal single-domain behavior. Transverse susceptibility measurements further quantified robust anisotropy fields that remain stable across varying temperatures. Dynamic magnetic studies using FMR revealed well-defined spectra with broad line shapes and temperature-independent g-factors, along with high damping, thus suggesting an efficient high-frequency energy dissipation and strong interfacial spin–orbit effects. Calorimetric magnetic hyperthermia studies, performed in both deionized water and agar media, consistently demonstrated that these nanocomposites are well suited for heating purposes. SAR values evaluated using multiple approaches (initial slope, Box–Lucas, Newton cooling), follow consistent trends. The observed quadratic dependence of SAR on H_0 and the calculated magnetic-field-invariant ILP confirms the system's operation within the LRT regime, with heat dissipation predominantly governed by relaxation-based mechanisms along with minor hysteresis contributions.

Together, these findings demonstrate the successful integration of magnetic cobalt-ferrite nanoparticles into a mesoporous activated carbon matrix, thus positioning CFO@C as a robust multifunctional nanomaterial platform. The observed magnetic hardness couple with multiphase switching, broadband loss characteristics, and structural confinement support its relevance for not only high-performance hyperthermia applications but also for future integration into technologies such as magnetically responsive inks, additive manufacturing platforms, and broadband EMI shielding. Future work may explore optimization of particle alignment, dispersion, and interfacial control within the carbon matrix to elevate its application potential in tunable and frequency-responsive behavior in next-generation multifunctional platforms.

4 | Experimental Section

4.1 | Chemicals and Materials Synthesis

A commercial AC was employed as a nano-template for the preparation of the cobalt ferrite nanoparticles. The AC material (M30), supplied by Osaka Gas company (Japan), has a large Brunauer-Emmett-Teller (BET) surface area of 2350 $m^2 \cdot g^{-1}$, a high pore volume of 1.47 $cm^3 \cdot g^{-1}$ and a porosity composed of mesopores with diameters up to 6 − 7 nm in diameter. The synthesis route is based on the pyrolysis occurring within the restricted volume formed by the AC porosity. In a typical fabrication procedure to obtain CFO nanoparticles embedded in a porous carbon matrix, 1 g of AC was impregnated under continuous stirring with a solution formed by a stoichiometric mixing of cobalt nitrate [$Co(NO_3)_2$] and iron nitrate [$Fe(NO_3)_3$], ensuring thorough wetting and capillary filling of the porous framework. The process takes place in the presence of ethanol up to the incipient wetness point and then dried at 50°C for 2 h. Subsequently, the composite was impregnated with ethylene glycol as a complexing agent to improve precursor dispersion and promote homogeneity. Then, the mixture was heat treated under a N_2 atmosphere up to 80°C and maintained at this temperature for 1 h. The final nanocomposite powder samples are obtained after a subsequent thermal treatment (pyrolysis) at target temperatures: 300°C and 350°C for 2 h. These samples will hereafter be referred to as M-300 and M-350, respectively. The

CFO loading in the final composite was estimated to be ∼ 20 wt.% as deduced from thermogravimetric analysis (TGA). A schematic sketch of the synthesis protocol is provided in Figure 1.

4.2 | Structural and Microstructural Characterizations

Room temperature X-ray powder diffraction (XRD) was used to identify the crystalline phases and to analyze the crystalline structure of the samples. The patterns were collected at room temperature in a Seifert XRD 3000 T/T diffractometer with Mo K_{α_1}(0.709 ∀) and K_{α_2} (0.713 ∀) radiations, in an angular range (2θ) of 10 − 30° in steps of 0.03° and a collection time of 30 s. The instrumental resolution of the diffractometer was determined using a standard LaB_6 sample. Detailed structural and crystallographic information was obtained from the full profile fitting of the XRD patterns using the FullProf suite package based on the Rietveld method, with rather good reliability factors, that is, the R-weighted pattern (R_{wp}) being below 5% [30].

The microstructure and morphology of the synthesized CFO@C nanocomposites was analyzed using Transmission Electron Microscopy (TEM) and high-resolution TEM (HRTEM) in the JEOL 200-EXII and a JEOL JEM-2100F microscopes, operated at accelerating voltages of 180 and 200 kV, respectively. For imaging purposes, the samples were prepared by first dispersing a small amount of powder in ethanol with the aid of an ultrasonic bath to ensure homogeneity, followed by drop-casting the resulting suspension onto carbon-coated copper grids and allowed to air-dry for several hours prior to imaging. The histograms corresponding to the nanoparticle size distributions were elaborated by measuring the diameters of thousands of randomly selected particles from multiple TEM images using ImageJ software, and modelled with a lognormal fit [31].

4.3 | Static Magnetic Measurements

Static magnetization measurements were carried out using the Quantum Design Vibrating Sample Magnetometer (VSM) option of the Physical Property Measurement System. For these measurements, the dried nanoparticle samples were carefully loaded into the VSM sample holder. Magnetization versus applied magnetic field (M(H)) measurements were conducted over a temperature range from 5 to 320 K to evaluate field-dependent magnetic behavior. Temperature-dependent magnetization (M(T)) measurements were performed under three standard protocols: zero-field-cooled (ZFC), field-cooled (FC), and field-cooled warming (FCW), spanning the temperature range of 5 to 350 K.

4.4 | Dynamic Magnetic Measurements

Dynamic magnetic behavior of the synthesized nanocomposites was investigated through calorimetric magnetic hyperthermia, broadband ferromagnetic resonance (FMR), and RF transverse susceptibility (TS) measurements, enabling evaluation across a broad frequency spectrum ranging from kHz to GHz regimes.

Calorimetric magnetic hyperthermia experiments were conducted using an Ambrell Easyheat LI3542 induction heating system (4.2 kW, 310 kHz; Ambrell, Rochester, NY, USA). The measurements were carried out in two different dispersion media: deionized water and 2% agarose gel, to assess heating performance under both fluidic and constrained environments. For each medium, two nanoparticle concentrations (0.5 and 1.0 mg/mL) were tested under three alternating magnetic field strengths: 400, 600, and 800 Oe. The temperature evolution of the samples was recorded in real-time, and the specific absorption rate (SAR) was extracted using multiple fitting approaches. To probe the high-frequency magnetic dynamics of the nanocomposites, FMR measurements were performed using a CryoFMR-40 assembly integrated with the Quantum Design PPMS. The measurements were carried out over a frequency window spanning 18–30 GHz. TS measurements were conducted using a custom-built RF tunnel-diode oscillator (TDO) circuit operating at a resonance frequency of 15 MHz (∼ 10 Oe). The experimental setup was interfaced with a Quantum Design PPMS DynaCool system to facilitate temperature-dependent and field-swept measurements.

4.5 | Statistical Analysis

All magnetic characterization data were analyzed using standard fitting procedures appropriate for physical property measurements. Raw magnetometry, transverse susceptibility, ferromagnetic resonance (FMR), and hyperthermia datasets were preprocessed for plotting where required. Reported parameters such as particle size, blocking temperature, Bloch's exponent, effective anisotropy fields, g-factors, Gilbert damping, SAR and ILP were extracted from model-based fitting of experimental data.

No formal hypothesis testing or significance testing was applied, as the study focuses on quantitative parameter extraction rather than statistical comparison between populations. Data analysis and fitting were performed using software that included OriginPro, ImageJ and custom scripts written in Python.

Author Contributions

Shah Qasim Jan: Conceptualization, Methodology, Data curation (VSM, TS, FMR and Hyperthermia), Formal analysis, Writing: original draft, review & editing. **Rajeswari Roy Chowdhury**: Supervision, Methodology, Investigation, Writing: review & editing. **Noah Schulz**: Software development (deconvolution of hysteresis loops and FMR analysis), Writing: review & editing. **Ayomipo Israel Ojo**: Investigation (FMR measurements). **Darío A. Arena** (*Corresponding Author # 2*): Supervision, Resources (Characterizations), Funding acquisition (NSF). **Hariharan Srikanth** (*Corresponding Author # 1*): Supervision, Project administration, Resources (Characterizations), Funding acquisition (DOE). **María González de la Vega**: Sample synthesis and preparation, Data curation (XRD and TEM imaging analysis), Writing: review & editing. **Jesus A. Blanco**: Supervision, Resources (Characterizations), Funding acquisition. **Pedro Gorria** (*Corresponding Author # 3*): Supervision, Resources (sample preparation, synthesis and characterizations), Project administration, Funding acquisition.

Acknowledgements

Work at USF (magnetic characterization and the respective analysis) supported by Department of Energy, Office of Basic Energy Sciences,

Division of Materials Science and Engineering under Award No. DE-FG02-07ER46438. SQJ, DAA, and HS acknowledge the support of the National Science Foundation under award No. DMR-2327667. N.S would like to acknowledge funding from the US Department of Defense SMART program and the Naval Innovative Science and Engineering Program. Work at the University of Oviedo is supported by PID2023-150968OA-I00 and PID2022-138256NB-C21 from AEI (Spanish Research Agency) and ERDF, UE; and SEK-25-GRU-GIC-24-113 from SEKUENS (Research Agency of the Principality of Asturias). The authors also thank XRD and TEM labs at the SCTs (University of Oviedo) for technical support. Work at University of South Florida: US Department of Energy (DOE): DE-FG02-07ER46438. National Science Foundation (NSF): DMR-2327667. Work at the University of Oviedo: Spanish AEI: PID2023-150968OA-I00 and PID2022-138256NB-C21. Principality of Asturias: SEK-25-GRU-GIC-24-113.

Funding

Work at University of South Florida: US Department of Energy (DOE): DE-FG02-07ER46438, National Science Foundation (NSF): DMR-2327667. Work at the University of Oviedo: Spanish AEI: PID2023-150968OA-I00 and PID2022-138256NB-C21, Principality of Asturias: SEK-25-GRU-GIC-24-113.

Conflicts of Interest

The authors declare no conflict of interest.

Data Availability Statement

The data that support the findings of this study are available from the corresponding author upon reasonable request.

References

1. V. Popova, E. Dmitrienko, and A. Chubarov, "Magnetic Nanocomposites and Imprinted Polymers for Biomedical Applications of Nucleic Acids," *Magnetochemistry* 9, no. 1 (2022): 12, https://doi.org/10.3390/magnetochemistry9010012.

2. S. Mourdikoudis, A. Kostopoulou, and A. P. LaGrow, "Magnetic Nanoparticle Composites: Synergistic Effects and Applications," *Advanced Science* 8, no. 12 (2021): 2004951, https://doi.org/10.1002/advs.202004951.

3. T. Dippong, E. A. Levei, and O. Cadar, "Recent Advances in Synthesis and Applications of MFe_2O_4 (M = Co, Cu, Mn, Ni, Zn) nanoparticles," *Nanomater* 11, no. 6 (2021): 1560.

4. P. Bardapurkar, S. Dalvi, V. Joshi, et al., "Effect of Silica Matrix on Structural and Optical Properties of Cobalt Ferrite Nanoparticles," *Results in Surfaces and Interfaces* 8 (2022): 100081, https://doi.org/10.1016/j.rsurfi.2022.100081.

5. S. H. Lim, T. W. Wong, and W. X. Tay, "Overcoming Colloidal Nanoparticle Aggregation in Biological Milieu for Cancer Therapeutic Delivery: Perspectives of Materials and Particle Design," *Advances in Colloid and Interface Science* 325 (2024): 103094, https://doi.org/10.1016/j.cis.2024.103094.

6. H. Wang, C. Liu, X. Yang, et al., "In Situ Synthesis of $CoFe_2O_4$ Nanoparticles Embedded in N-Doped Carbon Nanotubes for Efficient Electrocatalytic Oxygen Reduction Reaction," *International Journal of Hydrogen Energy* 47, no. 9 (2022): 6059–6066, https://doi.org/10.1016/j.ijhydene.2021.11.220.

7. H. T. Nguyen, J. Lee, E. Kwon, et al., "Metal-Complexed Covalent Organic Frameworks Derived N-Doped Carbon Nanobubble–Embedded Cobalt Nanoparticle as a Magnetic and Efficient Catalyst for Oxone Activation," *Journal of Colloid and Interface Science* 591 (2021): 161–172, https://doi.org/10.1016/j.jcis.2021.01.108.

8. H. Wei, T. Lei, L. Ma, and W. Li, "Aramid Nanofiber-Reinforced Carbon Nanotubes@Cobalt Ferrite Nanoparticles Aerogel Films Achieve Excellent Electromagnetic Interference Shielding, Photothermal and Joule Heating Performance," *Ceramics International* 50, no. 23 (2024): 50388–50396, https://doi.org/10.1016/j.ceramint.2024.09.384.

9. R. Sadek, M. S. Sharawi, C. Dubois, H. Tantawy, and J. Chaouki, "Reduced Graphene Oxide/Barium Ferrite Ceramic Nanocomposite Synergism for High EMI Wave Absorption," *ACS Omega* 8, no. 17 (2023): 15099–15113, https://doi.org/10.1021/acsomega.2c08168.

10. F. Qin and C. Brosseau, "A Review and Analysis of Microwave Absorption in Polymer Composites Filled With Carbonaceous Particles," *Journal of Applied Physics* 111, no. 6 (2012): 061301.

11. S. Dhawan, K. Singh, A. Bakhshi, and A. Ohlan, "Conducting Polymer Embedded With Nanoferrite and Titanium Dioxide Nanoparticles for Microwave Absorption," *Synthetic Metals* 159, no. 21–22 (2009): 2259–2262, https://doi.org/10.1016/j.synthmet.2009.08.031.

12. R. C. Che, L. M. Peng, X. F. Duan, Q. Chen, and A. X. Liang, "Microwave Absorption Enhancement and Complex Permittivity and Permeability of Fe Encapsulated Within Carbon Nanotubes," *Advanced Materials* 16, no. 5 (2004): 401–405, https://doi.org/10.1002/adma.200306460.

13. N. Slepičková Kasálková, P. Slepička, and V. Švorčík, "Carbon Nanostructures, Nanolayers, and Their Composites," *Nanomaterials* 11, no. 9 (2021): 2368, https://doi.org/10.3390/nano11092368.

14. S. Sharma, M. Kaur, C. Sharma, A. Choudhary, and S. Paul, "Biomass-Derived Activated Carbon-Supported Copper Catalyst: An Efficient Heterogeneous Magnetic Catalyst for Base-Free Chan–Lam Coupling and Oxidations," *ACS Omega* 6, no. 30 (2021): 19529–19545, https://doi.org/10.1021/acsomega.1c01830.

15. N. Jayaprakash, K. Elumalai, S. Manickam, G. Bakthavatchalam, and P. Tamilselvan, "Carbon Nanomaterials: Revolutionizing Biomedical Applications With Promising Potential," *Nano Materials Science* (2024), https://doi.org/10.1016/j.nanoms.2024.11.004.

16. M. W. Alam, N. Allag, M. Naveed-Ur-Rehman, and S. Islam Bhat, "Graphene-Based Catalysts: Emerging Applications and Potential Impact," *The Chemical Record* 24, no. 11 (2024): 202400096, https://doi.org/10.1002/tcr.202400096.

17. T. Gong, L. Qin, W. Zhang, H. Wan, J. Lu, and H. Feng, "Activated Carbon Supported Palladium Nanoparticle Catalysts Synthesized by Atomic Layer Deposition: Genesis and Evolution of Nanoparticles and Tuning the Particle Size," *The Journal of Physical Chemistry C* 119, no. 21 (2015): 11544–11556, https://doi.org/10.1021/jp5130102.

18. S. Wang, J. Wang, X. Zhu, J. Wang, O. Terasaki, and Y. Wan, "Size-control Growth of Thermally Stable Au Nanoparticles Encapsulated Within Ordered Mesoporous Carbon Framework," *Chinese Journal of Catalysis* 37, no. 1 (2016): 61–72, https://doi.org/10.1016/S1872-2067(15)60917-2.

19. A. Bähr, H. Petersen, and H. Tüysüz, "Large-Scale Production of Carbon-Supported Cobalt-Based Functional Nanoparticles for Oxygen Evolution Reaction," *Chemcatchem* 13, no. 17 (2021): 3824–3835, https://doi.org/10.1002/cctc.202100594.

20. M. Liu, G. Chen, G. Liang, Y. Qian, L. Yang, and R. Che, "Asymmetric Atomic Diffusion-Engineered Magnetic Nano-Interfaces for Enhanced Low-Frequency Electromagnetic Wave Attenuation," *Advanced Functional Materials* 35 (2025): 2508174, https://doi.org/10.1002/adfm.202508174.

21. M. Samet, A. Kallel, and A. Serghei, "Polymer Bilayers With Enhanced Dielectric Permittivity and Low Dielectric Losses by Maxwell–Wagner–Sillars Interfacial Polarization: Characteristic Frequencies and Scaling Laws," *Journal of Applied Polymer Science* 136, no. 22 (2019): 47551, https://doi.org/10.1002/app.47551.

22. X. Xiong, H. Zhang, H. Lv, et al., "Recent Progress in Carbon-Based Materials and Loss Mechanisms for Electromagnetic Wave Absorption," *Carbon* 219 (2024): 118834.

23. A. Houbi, Z. A. Aldashevich, Y. Atassi, Z. B. Telmanovna, M. Saule, and K. Kubanych, "Microwave Absorbing Properties of Ferrites and Their

Composites: A Review," *Journal of Magnetism and Magnetic Materials* 529 (2021): 167839, https://doi.org/10.1016/j.jmmm.2021.167839.

24. M. Fadel, F. J. Martín-Jimeno, M. P. Fernández-García, et al., "Untangling the Role of the Carbon Matrix in the Magnetic Coupling of Ni@C Nanoparticles With Mixed FCC/HCP Crystal Structures," *Journal of Materials Chemistry C* 11, no. 12 (2023): 4070–4080, https://doi.org/10.1039/D3TC00257H.

25. X. Jia, L. Zhang, Y. Tian, et al., "Synthesis of Large-Sized Spherical Co–C Alloys With Soft Magnetic Properties Though a High-Pressure Solid-State Metathesis Reaction," *RSC advances* 14, no. 11 (2024): 7490–7498.

26. S. Q. Jan, N. Schulz, R. Roy Chowdhury, et al., "Magnetization Dynamics in Cobalt-Decorated Cobalt Ferrite Nanocomposites: Implications for High-Frequency Electromagnetic Shielding," *ACS Applied Nano Materials* 8, no. 20 (2025): 10459–10470.

27. J. Wells, O. Kosch, and F. Wiekhorst, "Multi-Frequency Hyperthermia Characterisation via Calorimetry and AC Magnetometry Measurements," *Journal of Magnetism and Magnetic Materials* 563 (2022): 169992, https://doi.org/10.1016/j.jmmm.2022.169992.

28. J. A. Vásquez-Peralvo, A. Tamayo-Domínguez, G. Pérez-Palomino, J. M. Fernández-González, and T. Wong, "3D inductive Frequency Selective Structures Using Additive Manufacturing and Low-Cost Metallization," *Sensors* 22, no. 2 (2022): 552, https://doi.org/10.3390/s22020552.

29. A. Sukovienė, S. Ali, A. Jagminas, and S. Ramanavičius, "Magnetic Cobalt and Other Types of Ferrite Nanoparticles: Synthesis Aspects and Novel Strategies for Application in Wastewater Treatment (Review)," *Applied Sciences: Special Issue Applications of Nanoparticles in The Environmental Sciences* 15, no. 2 (2025): 1–34.

30. J. Rodríguez-Carvajal, "Recent Advances in Magnetic Structure Determination by Neutron Powder Diffraction," *Physica B: Condensed Matter* 192, no. 1-2 (1993): 55–69, https://doi.org/10.1016/0921-4526(93)90108-I.

31. C. A. Schneider, W. S. Rasband, and K. W. Eliceiri, "NIH Image to ImageJ: 25 Years of Image Analysis," *Nature methods* 9, no. 7 (2012): 671–675, https://doi.org/10.1038/nmeth.2089.

32. S. Mitra, P. S. Veluri, A. Chakraborthy, and R. K. Petla, "Electrochemical Properties of Spinel Cobalt Ferrite Nanoparticles With Sodium Alginate as Interactive Binder," *ChemElectroChem* 1, no. 6 (2014): 1068–1074.

33. C. C. Li and H. C. Zeng, "Cobalt (hcp) Nanofibers With Pine-Tree-Leaf Hierarchical Superstructures," *Journal of Materials Chemistry* 20, no. 41 (2010): 9187–9192, https://doi.org/10.1039/c0jm01621g.

34. M. Manjunatha, G. S. Reddy, K. J. Mallikarjunaiah, R. Damle, and K. P. Ramesh, "Determination of Phase Composition of Cobalt Nanoparticles Using 59Co Internal Field Nuclear Magnetic Resonance," *Journal of Superconductivity and Novel Magnetism* 32, no. 10 (2019): 3201–3209, https://doi.org/10.1007/s10948-019-5083-7.

35. Y. Chen, X. F. Zhang, A. J. Wang, Q. L. Zhang, H. Huang, and J. J. Feng, "Ultrafine Fe_3C Nanoparticles Embedded in N-doped Graphitic Carbon Sheets for Simultaneous Determination of Ascorbic Acid, Dopamine, Uric Acid and Xanthine," *Microchimica Acta* 186, no. 9 (2019): 660, https://doi.org/10.1007/s00604-019-3769-y.

36. K. L. Livesey, S. Ruta, N. Anderson, D. Baldomir, R. W. Chantrell, and D. Serantes, "Beyond the Blocking Model to Fit Nanoparticle ZFC/FC Magnetisation Curves," *Scientific Reports* 8, no. 1 (2018): 1–9, https://doi.org/10.1038/s41598-018-29501-8.

37. J. Du, B. Zhang, R. Zheng, and X. Zhang, "Memory Effect and Spin-Glass-Like Behavior in Co-Ag Granular Films," *Physical Review B* 75, no. 1 (2007): 014415, https://doi.org/10.1103/PhysRevB.75.014415.

38. H. Khurshid, P. Lampen-Kelley, Ò. Iglesias, et al., "Spin-Glass-Like Freezing of Inner and Outer Surface Layers in Hollow γ-Fe_2O_3 nanoparticles γ-Fe_2O_3 nanoparticles," *Scientific Reports* 5, no. 1 (2015): 15054, https://doi.org/10.1038/srep15054.

39. B. K. Chatterjee, C. Ghosh, and K. Chattopadhyay, "Temperature Dependence of Magnetization and Anisotropy in Uniaxial $NiFe_2O_4$ Nanomagnets: Deviation From the Callen-Callen Power Law," *Journal of Applied Physics* 116, no. 15 (2014).

40. B. Aslibeiki, G. Varvaro, D. Peddis, and P. Kameli, "Particle Size, Spin Wave and Surface Effects on Magnetic Properties of $MgFe_2O_4$ Nanoparticles," *Journal of Magnetism and Magnetic Materials* 422 (2017): 7–12, https://doi.org/10.1016/j.jmmm.2016.08.057.

41. S. K. Paswan, S. Kumari, M. Kar, et al., "Optimization of Structure-Property Relationships in Nickel Ferrite Nanoparticles Annealed at Different Temperature," *Journal of Physics and Chemistry of Solids* 151 (2021): 109928, https://doi.org/10.1016/j.jpcs.2020.109928.

42. K. Mandal, S. Mitra, and P. A. Kumar, "Deviation from Bloch T3/2 Law in Ferrite Nanoparticles," *Europhysics Letters* 75 (2006): 618.

43. K. Mandal, S. Mitra, and P. A. Kumar, "Deviation From Bloch $T^{3/2}$ Law in Ferrite Nanoparticles," *Europhysics Letters (EPL)* 75, no. 4 (2006): 618, https://doi.org/10.1209/epl/i2006-10148-y.

44. A. H. Morrish, *The* Physical Principles of Magnetism (Wiley, 2001), https://doi.org/10.1109/9780470546581.

45. R. Skomski and D. Leslie-Pelecky, "Cooperative Freezing in Spin Glasses and Magnetic Nanostructures," *Journal of Applied Physics* 89, no. 11 (2001): 7036–7038, https://doi.org/10.1063/1.1358337.

46. G. M. Alzoubi, A. S. Masadeh, and M. Shatnawi, "Investigation of the Structural, Morphological, and Magnetic Properties of Small Crystalline Co–Cu Ferrite Nanoparticles in the Single-Domain Regime," *AIP Advances* 12, no. 6 (2022): 065101, https://doi.org/10.1063/5.0087446.

47. C. Nayek, K. Manna, G. Bhattacharjee, P. Murugavel, and I. Obaidat, "Investigating Size-and Temperature-dependent Coercivity and Saturation Magnetization in PEG Coated Fe_3O_4 Nanoparticles," *Magnetochemistry* 3, no. 2 (2017): 19, https://doi.org/10.3390/magnetochemistry3020019.

48. A. P. Roberts, Y. Cui, and K. L. Verosub, "Wasp-Waisted Hysteresis Loops: Mineral Magnetic Characteristics And Discrimination of Components in Mixed Magnetic Systems," *Journal of Geophysical Research: Solid Earth* 100, no. B9 (1995): 17909–17924, https://doi.org/10.1029/95JB00672.

49. L. Corbellini, J. Plathier, C. Lacroix, C. Harnagea, D. Ménard, and A. Pignolet, "Hysteresis Loops Revisited: An Efficient Method to Analyze Ferroic Materials," *Journal of Applied Physics* 123, no. 12 (2016): 120.

50. Q. Liu, Q. Cao, and H. Bi, "CoNi@SiO_2@TiO_2 and CoNi@Air@TiO_2 microspheres with strong wideband microwave absorption," *Advanced Materials* 28 (2016), 486–490.

51. P. Poddar, M. B. Morales, N. A. Frey, S. A. Morrison, E. E. Carpenter, and H. Srikanth, "Transverse Susceptibility Study of the Effect of Varying Dipolar Interactions on Anisotropy Peaks in a Three-dimensional Assembly of Soft Ferrite Nanoparticles," *Journal of Applied Physics* 104, no. 6 (2008), https://doi.org/10.1063/1.2977592.

52. G. Asti and S. Rinaldi, "Nonanaliticity of the Magnetization Curve: Application to the Measurement of Anisotropy in Polycrystalline Samples," *Physical Review Letters* 28, no. 24 (1972): 1584, https://doi.org/10.1103/PhysRevLett.28.1584.

53. I. Benguettat-El Mokhtari and D. Schmool, "Ferromagnetic Resonance in Magnetic Oxide Nanoparticules: A Short Review of Theory and Experiment," *Magnetochemistry* 9, no. 8 (2023): 191, https://doi.org/10.3390/magnetochemistry9080191.

54. N. Usov and O. Serebryakova, "Deconvolution of Ferromagnetic Resonance Spectrum of Magnetic Nanoparticle Assembly Using Genetic Algorithm," *Scientific Reports* 12, no. 1 (2022): 3126, https://doi.org/10.1038/s41598-022-07105-7.

55. A. G. Gurevich and G. A. Melkov, *Magnetization Oscillations and Waves* (CRC Press, 2020), https://doi.org/10.1201/9780138748487.

56. E. De Biasi, C. A. Ramos, A. Butera, and R. D. Zysler, "Effect of Thermal Fluctuations in FMR Experiments in Uniaxial Magnetic Nanoparticles: Blocked vs. superparamagnetic Regimes," *Journal of Magnetism and Magnetic Materials* 326 (2013): 138–146, https://doi.org/10.1016/j.jmmm.2012.08.046.

57. E. Wetterskog, A. Castro, L. Zeng, et al., "Size and Property Bimodality in Magnetic Nanoparticle Dispersions: Single Domain Particles vs. Strongly Coupled Nanoclusters," *Nanoscale* 9, no. 12 (2017): 4227–4235, https://doi.org/10.1039/C7NR00023E.

58. D. Schmool and M. Schmalzl, "Ferromagnetic Resonance in Magnetic Nanoparticle Assemblies," *Journal of Non-Crystalline Solids* 353, no. 8–10 (2007): 738–742, https://doi.org/10.1016/j.jnoncrysol.2006.12.095.

59. A. Chanda, C. Holzmann, N. Schulz, et al., "Temperature Evolution of Magnon Propagation Length in $Tm_3Fe_5O_{12}$ Thin Films: Roles of Magnetic Anisotropy and Gilbert Damping," *ACS nano* 18, no. 9 (2024): 7223–7240, https://doi.org/10.1021/acsnano.3c12495.

60. G. Woltersdorf, *Spin-Pumping and Two-Magnon Scattering in Magnetic Multilayers* (Sinon Fraser University, 2004).

61. C. Kittel and P. McEuen, *Introduction to Solid state Physics* (John Wiley & Sons, 2018).

62. P. Hernández-Gómez, M. Valente, M. Graça, and J. Muñoz, "Synthesis, Structural Characterization and Broadband Ferromagnetic Resonance in Li Ferrite Nanoparticles," *Journal of Alloys and Compounds* 765 (2018): 186–192, https://doi.org/10.1016/j.jallcom.2018.06.172.

63. E. Burzo and R. Baican, "Thermal Variation of G Values in YFe_2 and $GdCo_2$ Compounds," *Solid State Communications* 18, no. 11-12 (1976): 1475–1477, https://doi.org/10.1016/0038-1098(76)90373-2.

64. H. Beljers and D. Polder, "Magnetization in Ferrites: G-Factors in Ferrite Materials," *Nature* 165, no. 4203 (1950): 800–800, https://doi.org/10.1038/165800a0.

65. D. J. Griffiths, *Introduction to Electrodynamics* (Cambridge University Press, 2023), https://doi.org/10.1017/9781009397735.

66. M. Müller, J. Weber, S. T. Goennenwein, et al., "Temperature Dependence of the Magnon-Phonon Interaction in Hybrids of High-Overtone Bulk Acoustic Resonators With Ferromagnetic Thin Films," *Physical Review Applied* 21, no. 3 (2024): 034032, https://doi.org/10.1103/PhysRevApplied.21.034032.

67. Y. Kim, H. An, and S. K. Kim, "Role of Spin–Orbit Coupling in Spin-to-Lattice Energy Conversion in Ferrite Nanoparticles," *Scientific Reports* 15, no. 1 (2025): 42469, https://doi.org/10.1038/s41598-025-26520-0.

68. I. Nlebedim, Y. Melikhov, and D. C. Jiles, "Temperature Dependence of Magnetic Properties of Heat Treated Cobalt Ferrite," *Journal of Applied Physics* 115, no. 4 (2014), https://doi.org/10.1063/1.4862300.

69. Q. Song and Z. J. Zhang, "Correlation Between Spin−Orbital Coupling and the Superparamagnetic Properties in Magnetite and Cobalt Ferrite Spinel Nanocrystals," *The Journal of Physical Chemistry B* 110, no. 23 (2006): 11205–11209, https://doi.org/10.1021/jp060577o.

70. B. K. Kuanr, S. R. Mishra, L. Wang, et al., "Frequency and Field Dependent Dynamic Properties of $CoFe_{2-x}Al_xO_4$ ferrite nanoparticles," *Materials Research Bulletin* 76 (2016): 22–27, https://doi.org/10.1016/j.materresbull.2015.11.033.

71. G. Datt, C. Kotabage, and A. C. Abhyankar, "Ferromagnetic Resonance of $NiCoFe_2O_4$ Nanoparticles and Microwave Absorption Properties of Flexible $NiCoFe_2O_4$ –Carbon Black/Poly(Vinyl Alcohol) Composites," *Physical Chemistry Chemical Physics* 19, no. 31 (2017): 20699–20712, https://doi.org/10.1039/C7CP03953K.

72. M. Dabla, M. Sharma, and B. K. Kuanr, "Transition From Hard to Soft Co-Ni Ferrites With Cr Incorporation: Novel Insights Into Cation Distribution and Ferromagnetic Resonance," *Journal of Magnetism and Magnetic Materials* 614 (2025): 172746, https://doi.org/10.1016/j.jmmm.2024.172746.

73. S. Chen, M. Tang, Z. Zhang, B. Ma, S. Lou, and Q. Jin, "Interfacial Effect on the Ferromagnetic Damping of CoFeB Thin Films With Different Under-Layers," *Applied Physics Letters* 103, no. 3 (2013): 032402.

74. D. Mazumdar, K. Das, and I. Das, "Magnetic Exchange Coupled Composite Behavior in the Doped Manganite Nanoparticles: A Proposed Phenomenological Model," *Physica B: Condensed Matter* 695 (2024): 416476, https://doi.org/10.1016/j.physb.2024.416476.

75. E. Barati and M. Cinal, "Gilbert Damping in Binary Magnetic Multilayers," *PhRvB* 95, no. 13 (2017): 134440.

76. B. Issa, I. M. Obaidat, B. A. Albiss, and Y. Haik, "Magnetic Nanoparticles: Surface Effects and Properties Related to Biomedicine Applications," *International Journal of Molecular Sciences* 14, no. 11 (2013): 21266–21305, https://doi.org/10.3390/ijms141121266.

77. I. Barsukov, H. Lee, A. Jara, et al., "Giant Nonlinear Damping in Nanoscale Ferromagnets," *Science Advances* 5, no. 10 (2019): aav6943, https://doi.org/10.1126/sciadv.aav6943.

78. E. Barati, M. Cinal, D. Edwards, and A. Umerski, "Gilbert Damping in Magnetic Layered Systems," *PhRvB* 90, no. 1 (2014): 014420.

79. C. Iacovita, G. F. Stiufiuc, R. Dudric, et al., "Saturation of Specific Absorption Rate for Soft and Hard Spinel Ferrite Nanoparticles Synthesized by Polyol Process," *Magnetochemistry* 6, no. 2 (2020): 23, https://doi.org/10.3390/magnetochemistry6020023.

80. E. A. Perigo, G. Hemery, O. Sandre, et al., "Fundamentals and Advances in Magnetic Hyperthermia," *Applied Physics Reviews* 2, no. 4 (2015): 041302, https://doi.org/10.1063/1.4935688.

81. I. Andreu, E. Natividad, L. Solozabal, and O. Roubeau, "Nano-objects for Addressing the Control of Nanoparticle Arrangement and Performance in Magnetic Hyperthermia," *ACS nano* 9, no. 2 (2015): 1408–1419, https://doi.org/10.1021/nn505781f.

82. S. Kumari, M. K. Manglam, L. K. Pradhan, L. Kumar, J. Borah, and M. Kar, "Modification in Crystal Structure of Copper Ferrite Fiber by Annealing and its Hyperthermia Application," *Applied Physics A* 127 (2021): 1–13.

83. D. Lachowicz, W. Górka, A. Kmita, et al., "Enhanced Hyperthermic Properties of Biocompatible Zinc Ferrite Nanoparticles With a Charged Polysaccharide Coating," *Journal of Materials Chemistry B* 7, no. 18 (2019): 2962–2973, https://doi.org/10.1039/C9TB00029A.

84. R. E. Rosensweig, "Heating Magnetic Fluid With Alternating Magnetic Field," *Journal of Magnetism and Magnetic Materials* 252 (2002): 370–374, https://doi.org/10.1016/S0304-8853(02)00706-0.

85. O. Lemine, M. Elansary, S. Algessair, et al., "Enhanced In-Vitro Magnetic Hyperthermia Performance of Chitosan-Coated $CoFe_2O_4$ Nanoparticles," *Materials Today Communications* 46 (2025): 112852, https://doi.org/10.1016/j.mtcomm.2025.112852.

86. A. Omelyanchik, M. Salvador, F. D'orazio, et al., "Magnetocrystalline and Surface Anisotropy in $CoFe_2O_4$ Nanoparticles," *Nanomaterials* 10, no. 7 (2020): 1288, https://doi.org/10.3390/nano10071288.

87. K. Shen, Y. Yan, W. Gao, et al., "Heat-Generating $Mn_{0.5}Zn_{0.5}Fe_2O_4$/MWCNTs Nanocomposites for Enhancing Hyperthermia Efficacy in Magnetic Hyperthermia Applications," *Journal of Alloys and Compounds* 926 (2022): 166806, https://doi.org/10.1016/j.jallcom.2022.166806.

88. P. Seal, A. Alam, and J. P. Borah, "Tailoring Magnetic Properties of Fe_3O_4 Nanocomposites With Amine-Functionalized MWCNT for Optimal Hyperthermia Performance," *Materials Chemistry and Physics* 331 (2025): 130169, https://doi.org/10.1016/j.matchemphys.2024.130169.

89. P. Seal, C. Borgohain, N. Paul, P. D. Babu, and J. P. Borah, "Effect of Annealing in Tuning Magnetic Hyperthermic Efficiency of MWCNT/$CoFe_2O_4$ Nanocomposites," *Journal of Physics D: Applied Physics* 53, no. 37 (2020): 375002, https://doi.org/10.1088/1361-6463/ab8de5.

90. S. O. Solopan, N. Nedelko, S. Lewińska, et al., "Core/Shell Architecture as an Efficient Tool to Tune DC Magnetic Parameters and AC Losses in Spinel Ferrite Nanoparticles," *Journal of Alloys and Compounds* 788 (2019): 1203–1210, https://doi.org/10.1016/j.jallcom.2019.02.276.

91. A. Tiwari, N. C. Verma, S. Turkkan, et al., "Graphitic Carbon Coated Magnetite Nanoparticles for Dual Mode Imaging and Hyperthermia," *ACS Applied Nano Materials* 3, no. 1 (2019): 896–904, https://doi.org/10.1021/acsanm.9b02501.

92. A. Kotoulas, C. Dendrinou-Samara, C. Sarafidis, et al., "Carbon-Encapsulated Cobalt Nanoparticles: Synthesis, Properties, and Magnetic Particle Hyperthermia Efficiency," *Journal of Nanoparticle Research* 19, no. 12 (2017): 399, https://doi.org/10.1007/s11051-017-4099-9.

93. T. Şimşek, M. Keleş, E. F. Uçar, et al., "Graphitic Carbon-Coated FeCo Nanoparticles for Enhanced Magnetic Hyperthermia Therapy," *Physica Status Solidi (b)* (2025): 202500393.

94. A. Zeleňáková, Ľ. Nagy, P. Hrubovčák, et al., "Cobalt-Ferrite Nano-Cubes for Magnetic Hyperthermia Applications," *Journal of Alloys and Compounds* 989 (2024): 174415.

Supporting Information

Additional supporting information can be found online in the Supporting Information section.

Supporting File: adfm74340-sup-0001-SuppMat.docx.

Carbon Confinement as a Design Principle for Multiphase Magnetic Nanocomposites with Broadband Functionality

Shah Qasim Jan[1], Rajeswari Roy Chowdhury[1], Noah Schulz[2], Ayomipo Israel Ojo[1], María González de la Vega[3], Jesús A. Blanco[3], Pedro Gorria[3, 4], Darío A. Arena[1*] and Hariharan Srikanth[1*]*

[1]Department of Physics, University of South Florida, Tampa FL 33620, USA.
[2]Naval Surface Warfare Center, Panama City Division, Panama City 32407, USA.
[3]Departamento de Física, Universidad de Oviedo, 33007, Oviedo, Spain.
[4]IUTA, Universidad de Oviedo, 33203 Gijón, Spain.
*sharihar@usf.edu
*darena@usf.edu
*pgorria@uniovi.es

Supporting Information

1. EDX data

EDX analysis confirms a near-stoichiometric Co-deficient cobalt ferrite composition, approximated as $Co_{0.9}Fe_2O_4$, for both samples within the experimental uncertainty (**Table S1**).

Table S1. Atomic element composition of the M-300 and M-350 investigated samples.

Sample	***M-300***	***M-350***
C (%)	83.1	83.6
O (%)	14.7	14.5
Fe (%)	1.5	1.3
Co (%)	0.7	0.6

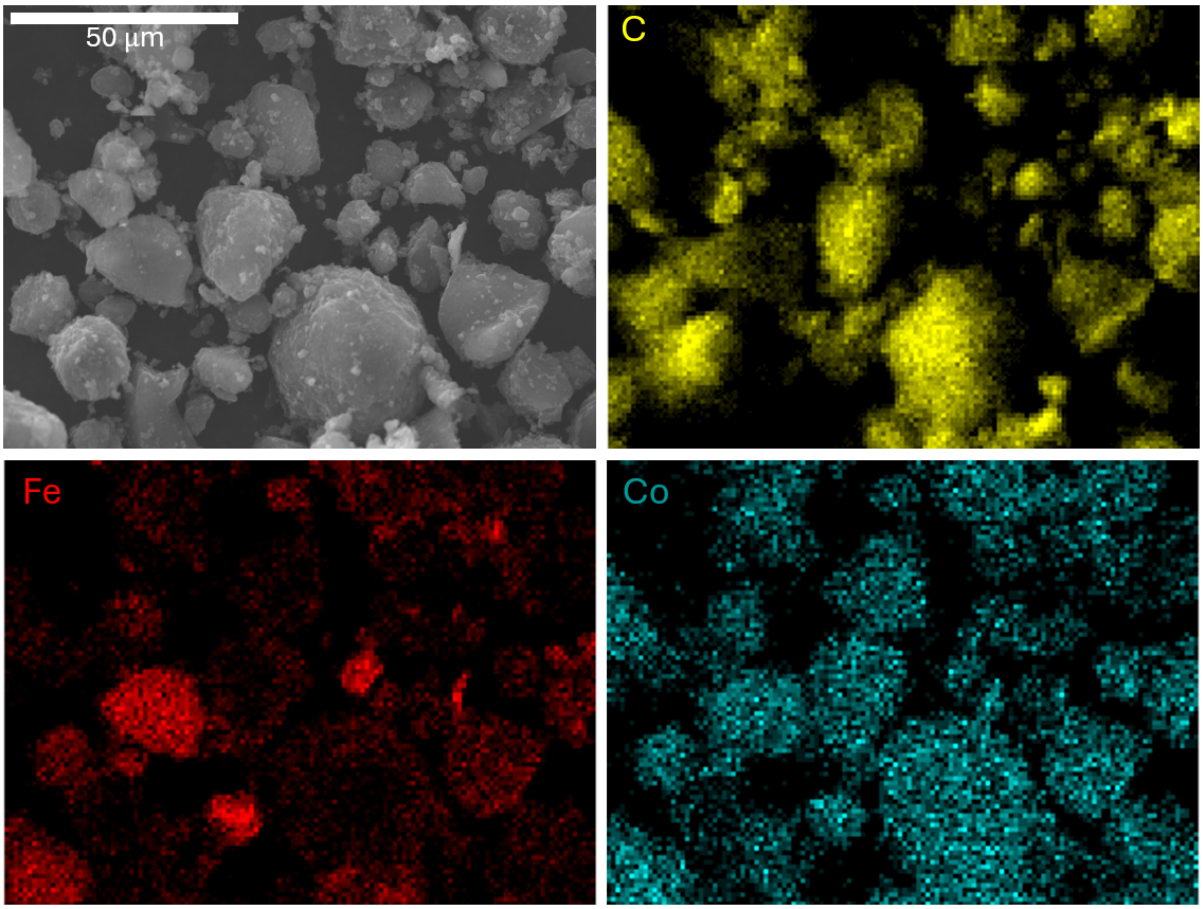

Figure S1. SEM micrograph and corresponding EDX elemental maps illustrating the spatial distribution of carbon (yellow), iron (red), and cobalt (blue) in the sample.

2. Magnetometry

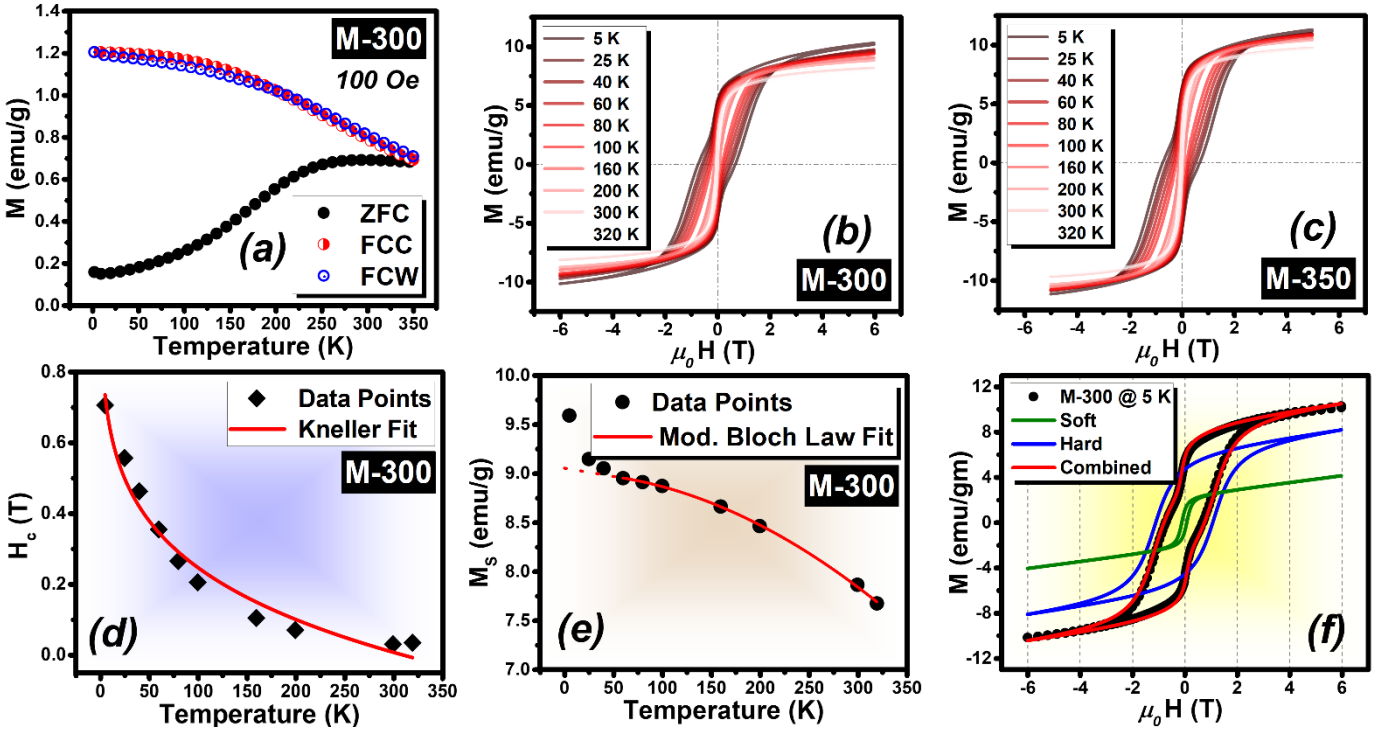

Figure S2: (a) Temperature-dependent magnetization $(M(T))$ for the $M-300$ sample measured under ZFC, FC and FCW protocols. **(b, c)** Magnetization versus field $(M(H))$ loops acquired at various temperatures $(5-320\,K)$ for $M-300$ and $M-350$, respectively. **(d)** Kneller law fitting of coercivity (H_C) as a function of temperature for $M-300$. **(e)** Bloch law fitting of saturation magnetization $(Ms\ vs.T)$ data for $M-300$. **(f)** Deconvolution of the $M(H)$ loop for $M-300$ showing hard and soft magnetic phase contributions.

3. Transverse Susceptibility Measurements

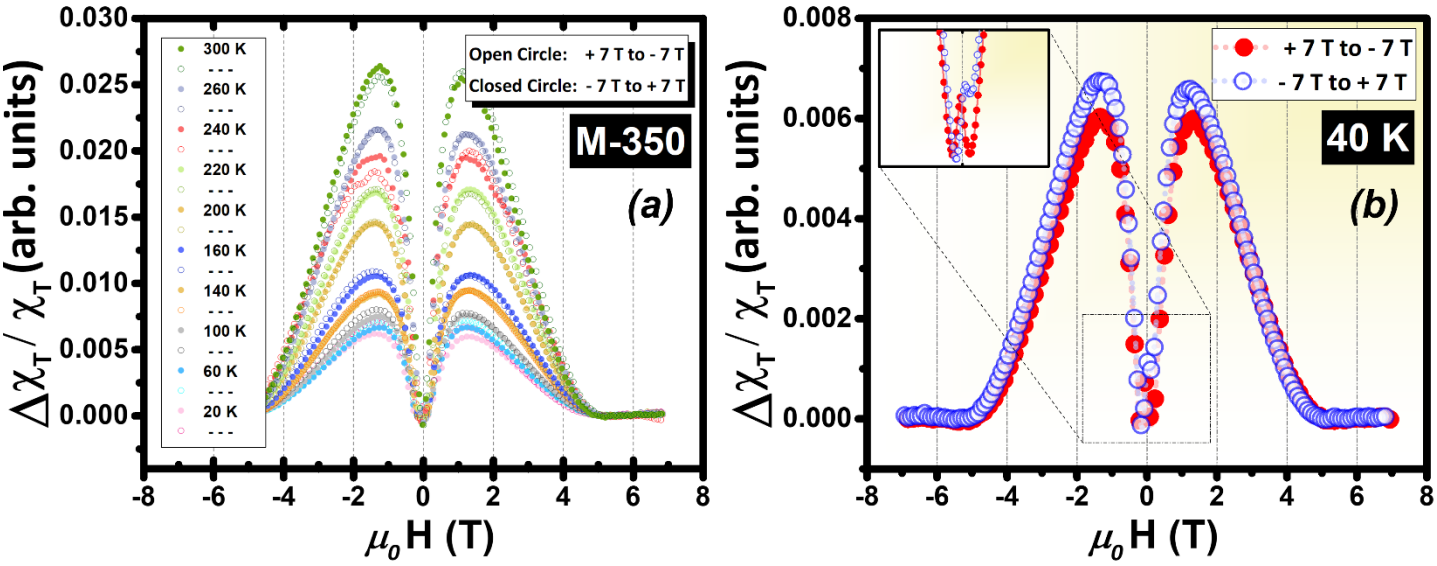

Figure S3: (a) Transverse susceptibility (TS) curves acquired across the temperature range of 20–300 K, highlighting temperature-dependent evolution of anisotropy features. **(b)** Representative TS curve at 40 K with a zoomed-in inset, revealing multiphase switching characteristics near zero field.

4. Ferromagnetic Resonance

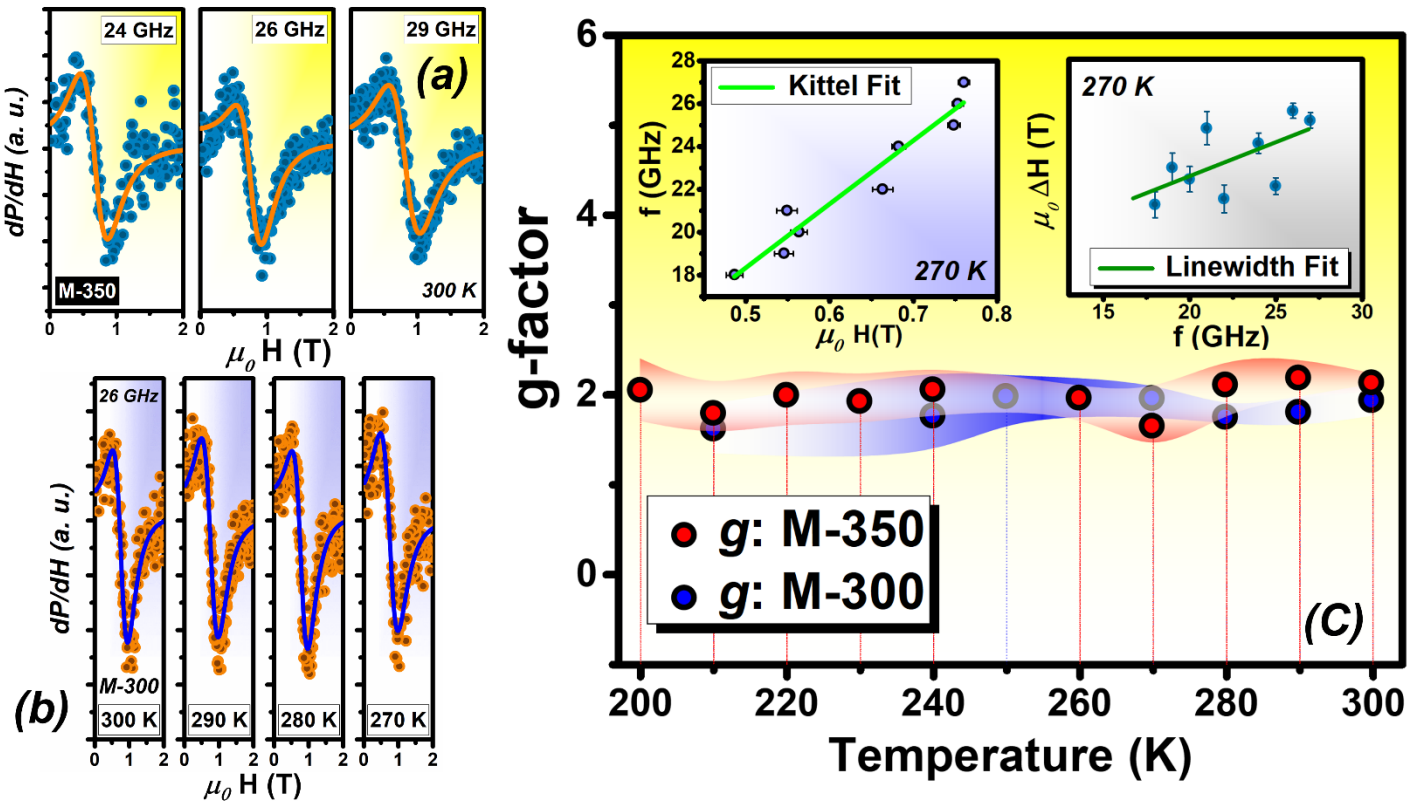

Figure S4: (a) Ferromagnetic resonance (FMR) spectra of the $M-300$ sample at $300\,K$ acquired across multiple frequencies ($18-30\,GHz$). **(b)** FMR line shapes recorded at a fixed frequency of $26\,GHz$ over a range of temperatures, illustrating the evolution of spectral broadening and resonance field shifts. **(c)** g-factor estimated by considering the in-plane model of the Kittel equation: $f = \frac{\gamma\mu_0}{2\pi}\sqrt{H_{res}\left(H_{res}+M_{eff}\right)}$ [S1]. The blue and red band of colors over the data points indicates the corresponding error in the estimated value of the g-factor at the respective temperature.

4.1. Estimation of the Dipolar Field Strength

To quantitatively rationalize the difference in the anisotropy fields derived from the FMR and TS measurements, we estimated the characteristic dipolar field B_{dip} acting on a nanoparticle due to its magnetic neighbors. The magnitude of this field was evaluated using the classical magnetic dipole approximation, expressed as [S2]:

$$B_{dip} = \left(\frac{\mu_0}{4\pi}\right)\cdot\left(\frac{M_S V}{r^3}\right) \qquad \text{S-1}$$

In the above expression, M_s is saturation magnetization; $V = (4/3)\pi r_P{}^3$ is the magnetic volume of the individual particle with radius r_P, and r represents the center-to-center distance between neighboring particles. The factor $\frac{\mu_0}{4\pi}$ (H/m) converts the field into SI units (T). Considering the CFO@C nanoparticles system here, the measured $M_s = 9.3\ emu/g$, which converts to SI units using the density of CFO ($\rho \approx 5.3\ g/cm^3$) to $4.9 \times 10^4 A/m$ [S3]. Substituting these quantities into the above relation and varying r to simulate different packing conditions gives the results summarized below in **Table S1**.

Table S2: Estimated dipolar field strength (B_{dip}) for CFO@C nanoparticles as a function of interparticle spacing.

Configuration	*r (nm)*	$B_{dip}\ (T)$	$B_{dip}\ (Oe)$
Dense (Touching)	8	2.56×10^{-3}	25.64
Moderately Dilute	13	5.98×10^{-4}	5.9762
Dilute	18	2.25×10^{-4}	2.25

As shown in **Figure S5**, the $1/r^3$dependence dictates that even small changes in interparticle separation leads to large variations in the local dipolar field. When particles are in closer proximity, as in the tightly packed TS sample, the enhanced dipolar coupling effectively augments the collective anisotropy, giving rise to higher values. Conversely, the FMR specimen, prepared as a more dilute and partially aligned layer, experiences significantly weaker dipolar fields, yielding lower apparent $H_A$value.

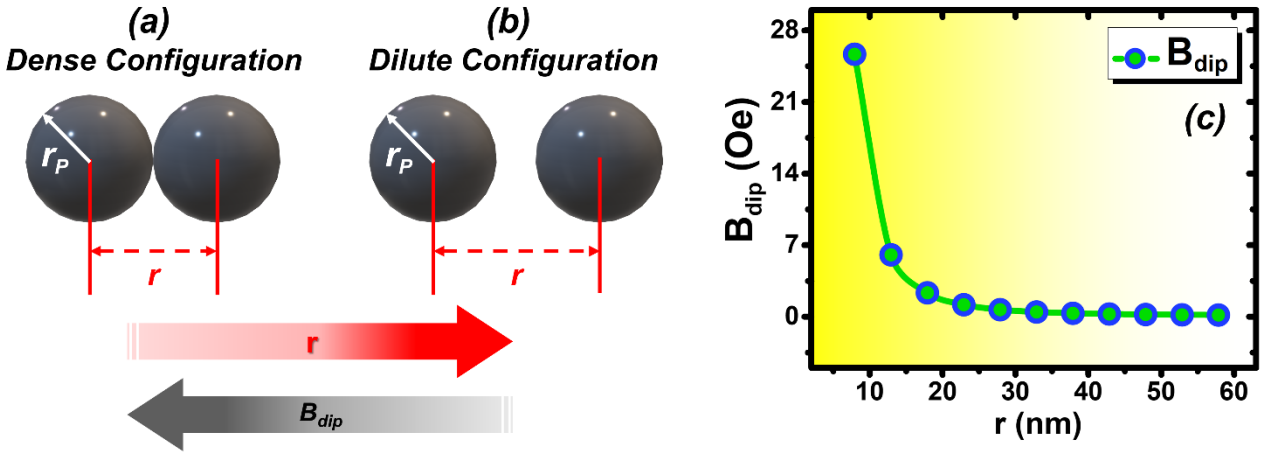

Figure S5: Schematic illustration of dipolar-field dependence on interparticle distance. **(a)** Dense configuration. **(b)** Dilute configuration. **(c)** Plot demonstrates the $B_{dip} \propto r^{-3}$

relationship, highlighting how small increases in interparticle distance sharply reduce the local dipolar field.

4.2. Estimation of Frequency Dependent Complex Permeability from FMR

The frequency-dependent complex permeability was evaluated using a phenomenological Landau–Lifshitz ferromagnetic resonance (LL-FMR) model, which describes the resonance-dominated magnetic response as [S4]:

$$\mu_{FMR}(f) = 1 + \left[\frac{\mu_s}{1+i{}^{f}/_{f_a} - \left({}^{f}/_{f_r}\right)^2}\right] \quad \text{S-2}$$

where $\mu_s = {}^{M_s}/_{H_A}$ is the static susceptibility term, f_r is the ferromagnetic resonance frequency, and f_a is the damping-related relaxation frequency. The frequency f corresponds to the probing microwave frequency.

For the M-350 sample, the parameters used in this calculation were obtained experimentally at 300 K as follows: the saturation magnetization $M_s = 10.7\ \text{emu.g}^{-1}$ from DC magnetometry, the effective anisotropy field $H_A = 0.11\ \text{T}$ from FMR analysis, and the Gilbert damping, $\alpha = 0.13$ from linewidth–frequency fitting. The gyromagnetic ratio was taken as $\gamma/2\pi = 0.0027\ \text{GHz.Oe}^{-1}$. Using these values, the characteristic frequencies were calculated as [S5]:

$$f_r = \gamma\sqrt{(M_s H_A)} \text{ and } f_a = {}^{\gamma H_A}/_{\alpha}\ .$$

Substituting these into Eq. (S-2), the real (μ') and imaginary (μ'') components of the permeability were evaluated with respect to frequency. As shown in **Figure S5**, the calculated $\mu'(f)$ and $\mu''(f)$ exhibit the characteristic dispersive behavior associated with ferromagnetic resonance [S6, S7]. At frequencies well below the resonance condition, μ' remains slightly greater than unity while μ'' increases gradually with frequency, reflecting the ability of the magnetization to follow the applied field and dissipate energy through damped precessional motion. Near the resonance frequency, μ'' reaches a pronounced maximum, accompanied by anomalous dispersion in μ', which decreases below unity due to the increasing phase lag between the magnetization and the driving field. At frequencies above resonance, both μ' and μ'' approach unity and zero, respectively, suggesting a transition to a weakly magnetic response regime where the magnetization cannot efficiently follow the high-frequency excitation. The broad nature of the resonance and loss peak reflects the high damping and multiphase magnetic

structure of the CFO@C nanocomposite, consistent with the experimentally observed FMR linewidths and exchange-coupled hard/soft phase coexistence.

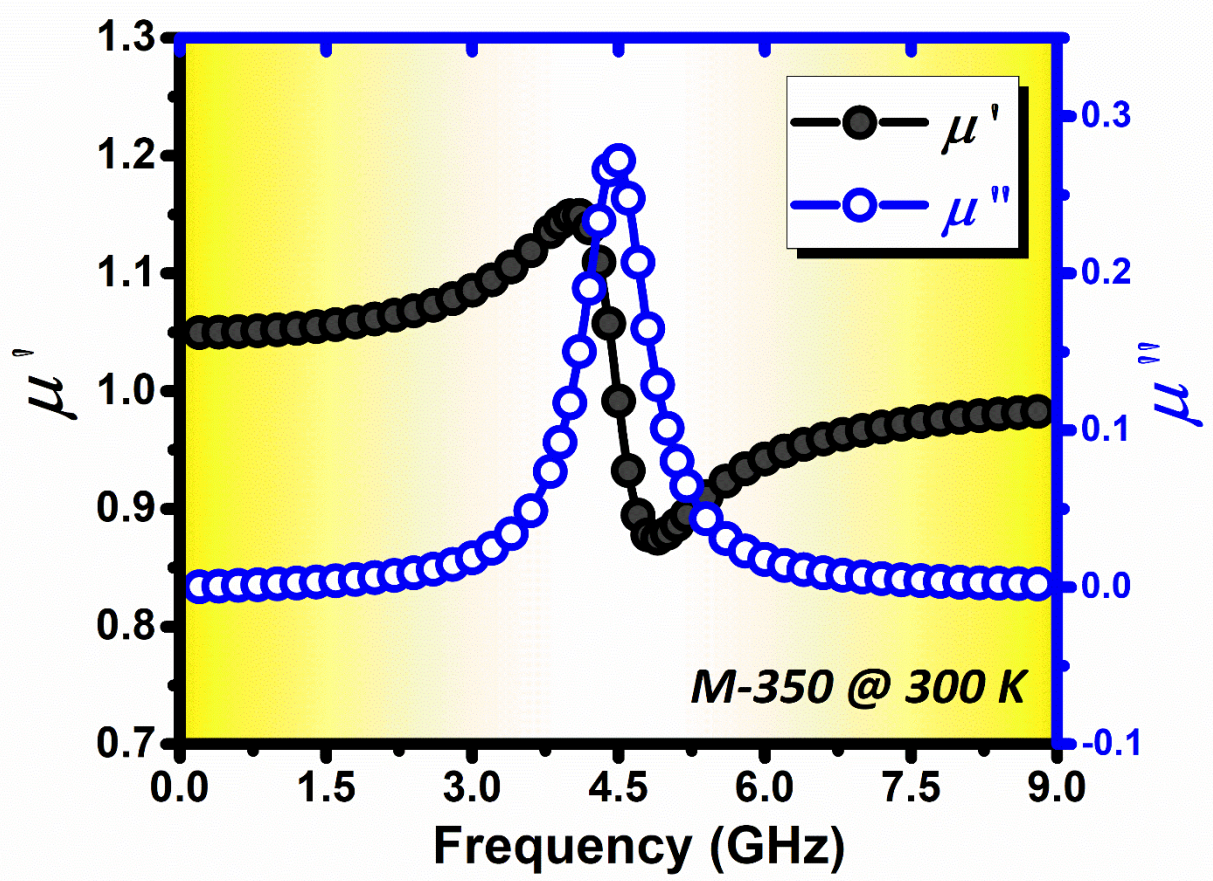

Figure S6: Frequency dependence of the real (μ') and imaginary (μ'') components of the complex magnetic permeability for the M-350 sample at 300 K, calculated using the LL-FMR-based phenomenological model (Eq. S-2).

It is important to emphasize that this LL-FMR-based calculation captures only the intrinsic, resonance-related magnetic contribution to permeability. It does not account for additional loss channels arising from interfacial exchange coupling, mesoscale magnetic inhomogeneity, conductive carbon pathways, or dielectric loss mechanisms, all of which contribute to the experimentally observed broadband absorption behavior. Accordingly, this analysis is intended to provide an order-of-magnitude estimate and qualitative insight into the high-frequency magnetic response, rather than a complete electromagnetic absorber model.

Table S3: Comparison of ferromagnetic resonance (FMR) parameters reported for representative nanoparticle systems. The table summarizes particle size, measurement frequency range (GHz), gyromagnetic ratio (γ), Gilbert damping parameter (α), anisotropy field (H_A), effective g-factor, and corresponding references.

System	Size (nm)	Frequency Range (GHz)	Gyromagnetic Ratio, γ ($\frac{GHz}{kOe}$)	Damping, α	Anisotropy Field, H_A	$g-Factor$	Ref.
$Cr\ doped$ $Co_{0.5}Ni_{0.5}Fe_2O_4$	~ 124 – 148	5 – 45	2.7 – 3.0	0.25 – 0.097	0.55 – 4.25 (kOe)	–	[S8]
$CoFe_{2-x}Al_xO_4$ (x: 0 – 0.9)	~ 58 – 82	1 – 55	–	0.18 – 0.35	–	–	[S9]
Dilute MNPs	~ 5 – 25	4.9 – 9.8	–	0.1 – 0.2	–	–	[S10]
Co Ni Ferrite NPs	~ 10 – 78	1.5 – 26	3.14	0.0128	–	2.2	[S11]
Fe_3O_4 $Ni_{0.5}Zn_{0.5}Fe_2O_4$ $Mn_{0.66}Zn_{0.34}Fe_2O_4$ (*Fluid*)	~ 9 – 10	0.1 – 6	–	0.15 0.20 0.12	46.07 4.65 27.49 (kA/m)	–	[S12]
$rGO/MnFe_2O_4$ (*VNA-FMR*)	–	5 – 30	2.84 – 2.90	0.12 – 0.15	–	–	[S13]
Fe_3O_4 $MnFe_2O_4$ $NiFe_2O_4$ (*VNA-FMR*)	~ 12 ($Core$) ~ 12 ($Shell$)	0.05 – 10	2.71 2.76 2.75	0.18 0.11 0.13	–	–	[S14]

5. Magnetic Hyperthermia

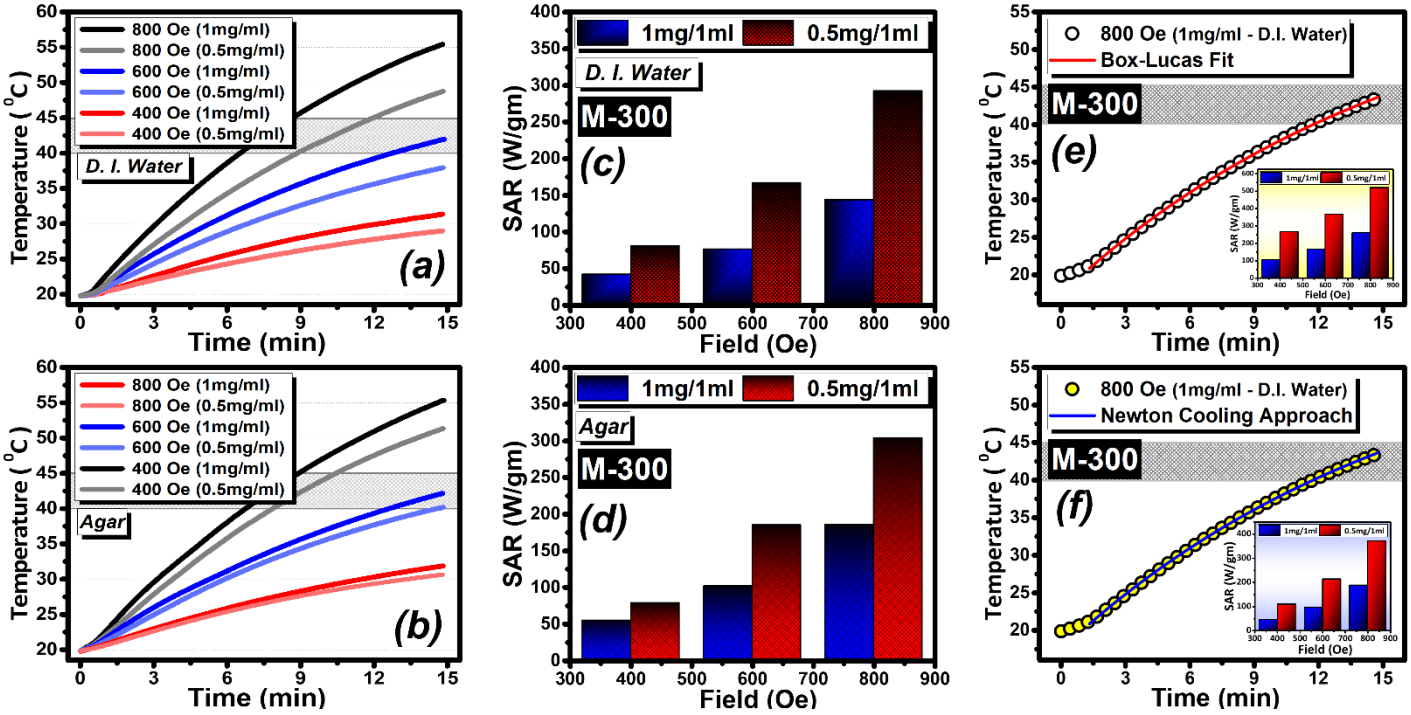

Figure S7: (a, b) Heating curves for the CFO@C ($M-350$) nanocomposites acquired at three field strengths ($400, 600,$ and $800\ Oe$) in two different media: DI water and agar, at concentrations of 0.5 and 1 mg/mL. **(c)** Specific Absorption Rate (SAR) values derived using the initial slope method, presented as bar graphs for comparative analysis. **(e, f)** Representative fits based on the Box–Lucas and Newton cooling approaches, respectively.

Table S4: Comparison of Specific Absorption Rate (SAR) values obtained for the $M-350$ sample using different approaches applied to the heating curves.

$M-350$ SAR Comparison (W/g)												
Field (Oe)	**Initial Slope Method**				**Newton Cooling Approach**				**Box-Lucas Approach**			
	D.I. Water		**Agar**		**D.I. Water**		**Agar**		**D.I. Water**		**Agar**	
	0.5 mg/ml	**1 mg/ml**	**0.5 mg/ml**	**1 mg/ml**	**0.5 mg/ml**	**1 mg/ml**	**0.5 mg/ml**	**1 mg/ml**	**0.5 mg/ml**	**1 mg/ml**	**0.5 mg/ml**	**1 mg/ml**
400	81.6	44.4	87.1	49.6	93.6	56.9	100.9	61.2	243.1	142.8	243.2	145.9
600	176.4	101.4	168.0	116.8	194.7	113.4	202.2	136.3	362.0	201.1	338.5	254.4
800	307.2	160.8	293.2	190.1	332.2	185.1	327.6	204.5	495.1	266.7	448.7	282.1

References

[S1] Kittel, C.; McEuen, P., *Introduction to solid state physics*. John Wiley & Sons: **2018.**

[S2] Griffiths, D. J., *Introduction to electrodynamics*. Cambridge University Press: **2023.**

[S3] Dedi; Idayanti, N.; Kristiantoro, T.; Alam, G. F. N.; Sudrajat, N., Magnetic properties of cobalt ferrite synthesized by mechanical alloying, *AIP Conference Proceedings, AIP Publishing LLC*, **2018**, p 020003.

[S4] Iakubov, I. T.; Lagarkov, A. N.; Maklakov, S. A.; Osipov, A. V.; Rozanov, K. N.; Ryzhikov, I. A.; Simonov, N. A.; Starostenko, S. N, Experimental study of microwave permeability of thin Fe films. *Journal of magnetism and magnetic materials*, **2003,** 258, 195-197.

[S5] Neo, C. P.; Yang, Y.; Ding, J., Calculation of complex permeability of magnetic composite materials using ferromagnetic resonance model. *Journal of Applied Physics*, **2010,** *107*(8).

[S6] Thalakkatukalathil, V. V., Electromagnetic modeling and characterization of anisotropic ferrite materials for microwave isolators/circulators (Doctoral dissertation, Université de Bretagne occidentale-Brest), **2017**.

[S7] Kang, L.; Zhao, Q.; Zhao, H.; Zhou, J., Magnetically tunable negative permeability metamaterial composed by split ring resonators and ferrite rods. *Optics express*, **2008,** *16*(12), 8825-8834.

[S8] Dabla, M.; Sharma, M.; Kuanr, B. K., Transition from hard to soft Co-Ni ferrites with Cr incorporation: Novel insights into cation distribution and ferromagnetic resonance. *Journal of Magnetism and Magnetic Materials*, 614, **2025**, 172746.

[S9] Kuanr, B. K.; Mishra, S. R.; Wang, L.; DelConte, D.; Neupane, D.; Veerakumar, V.; Celinski, Z., Frequency and field dependent dynamic properties of $CoFe_{2-x}Al_xO_4$ ferrite nanoparticles. *Materials Research Bulletin,* **2016,** 76, 22-27.

[S10] Usov, N. A.; Serebryakova, O. N., Deconvolution of ferromagnetic resonance spectrum of magnetic nanoparticle assembly using genetic algorithm. *Scientific Reports*, **2022,** *12*(1), 3126.

[S11] Lafta, S. H., Comparison of field sweep and frequency sweep evaluations of Co–Ni ferrite nanoparticles in the short circuit FMR method. *Kuwait Journal of Science*, **2024,** *51*(2), 100199.

[S12] Fannin, P. C.; Marin, C. N.; Malaescu, I.; Stefu, N., An investigation of the microscopic and macroscopic properties of magnetic fluids. *Physica B: Condensed Matter*, **2007,** *388*(1-2), 87-92.

[S13] Mishra, A.; Sharma, V.; Mohanty, T.; Kuanr, B. K, Microstructural and magnetic properties of rGO/$MnFe_2O_4$ nanocomposites; relaxation dynamics, *Journal of Alloys and Compounds*, **2019,** *790*, 983-991.

[S14] Lee, J. H., Kim, Y.; Kim, S. K., Highly efficient heat-dissipation power driven by ferromagnetic resonance in MFe_2O_4 (M = Fe, Mn, Ni) ferrite nanoparticles. *Scientific reports*, **2022,** *12*(1), 5232.